A novel retrieval of global dust optical depth and effective diameter based on MODIS thermal infrared observations

Jianyu Zheng, Hongbin Yu, Yaping Zhou, Yingxi Shi, Zhibo Zhang, Claudia Di Biagio, Paola Formenti, Alexander Smirnov

Remote Sensing of Environment 332 (2026) 115083

Contents lists available at ScienceDirect

Remote Sensing of Environment

journal homepage: www.elsevier.com/locate/rse

A novel retrieval of global dust optical depth and effective diameter based on MODIS thermal infrared observations

Jianyu Zheng [a,b,*], Hongbin Yu [b], Yaping Zhou [c,d], Yingxi Shi [a,b], Zhibo Zhang [a,e], Claudia Di Biagio [f], Paola Formenti [f], Alexander Smirnov [b,g]

[a] Goddard Earth Sciences Technology and Research II, University of Maryland at Baltimore County, Baltimore, MD, USA
[b] Earth Science Division, NASA Goddard Space Flight Center, Greenbelt, MD, USA
[c] Earth Resource Technology, College Park, MD, USA
[d] NOAA/NESDIS, Center for Satellite Application and Research, College Park, MD, USA
[e] Department of Physics, University of Maryland at Baltimore County, Baltimore, MD, USA
[f] Université Paris Cité and Univ Paris Est Creteil, CNRS, LISA, F-75013 Paris, France
[g] Science Systems and Applications, Inc., Lanham, MD, USA

ARTICLE INFO

Editor: Menghua Wang

Keywords:
Aerosol
Dust
Particle size distribution
Thermal infrared
MODIS
CALIOP

ABSTRACT

Airborne mineral dust significantly influences Earth's climate through perturbing Earth's radiation budget, modulating cloud formation and microphysical properties, and fertilizing the biosphere. Recent field campaigns have revealed substantially more coarse-mode dust particles in the atmosphere than previously recognized, yet current satellite retrievals and climate models inadequately represent these particles. This study presents a novel retrieval algorithm for dust aerosol optical depth at 10 μm ($AOD_{10\mu m}$) and effective diameter (Deff) using Moderate Resolution Imaging Spectroradiometer (MODIS) thermal infrared (TIR) observations over global land and ocean. Building upon the previous synergistic approach for MODIS and the Cloud-Aerosol Lidar with Orthogonal Polarization (CALIOP), we improve the retrieval from CALIOP-track-limited coverage to full-swath MODIS observations at 10-km resolution over both ocean and land surfaces. The retrieval improvements include: (1) application of climatological CALIOP dust vertical profiles (2007–2017) to constrain dust vertical distribution for off-CALIOP-track pixels; (2) the improved optimization method to effectively handle non-monotonic cost functions arising from temperature inversions within the Saharan Air Layer; and (3) extension to land surfaces through incorporation of MODIS-retrieved surface emissivity and ERA5 reanalysis data. Validation against coarse-mode AOD from global AERONET ($N = 4703$) and MAN ($N = 1673$) observations yields $R = 0.82$ and 0.85 for $AOD_{10\mu m}$, with retrieval uncertainty characterized as $\varepsilon = 15\% \times AOD + 0.04$. The retrieved Deff demonstrates excellent agreement with in-situ measurements collected from 24 field campaigns around the globe ($R = 0.84$, MBE = 0.23 μm, RMSE = 0.73 μm), capturing the particle size variation from near-source regions (Deff = 7–8 μm) to long-range transport (Deff = 3–5 μm). Case studies of dust events over the Namibian coast and trans-Atlantic corridor demonstrate the retrieval's capability to resolve episodic dust properties and size-dependent deposition during transport. This improved retrieval addresses the critical observational gap for coarse and super-coarse dust particles ($D > 5$ μm), providing essential constraints for dust life cycle studies and climate model evaluation.

1. Introduction

Airborne mineral dust (referred to as "dust"), mobilized through aeolian processes in arid and semi-arid regions, possesses the largest dry mass among the atmospheric aerosol species, which has critical impacts on our Earth systems (Choobari et al., 2014; Mahowald et al., 2014; Kok et al., 2023). The global transport of dust significantly influences Earth's radiative budget, atmospheric compositions, thermodynamic structures, and marine and terrestrial ecosystems. With particle sizes ranging from 0.001 to 100 μm, dust interacts with both shortwave solar and longwave terrestrial radiation, but the net radiative effect remains highly uncertain due to poorly constrained dust microphysical and mineralogical

* Corresponding author at: Goddard Earth Sciences Technology and Research II, University of Maryland at Baltimore County, Baltimore, MD, USA.
E-mail address: jzheng3@umbc.edu (J. Zheng).

https://doi.org/10.1016/j.rse.2025.115083
Received 15 July 2025; Received in revised form 26 September 2025; Accepted 8 October 2025

properties (Li et al., 2021). The absorption of both SW and LW radiation by dust increases the heating rate of the atmosphere, further impacting the atmospheric thermodynamic structures and consequently altering the cloud distribution (Miller and Tegen, 1998; Hansen et al., 1997; Tesfaye et al., 2015; Huang et al., 2006). Dust also interacts with clouds as both cloud condensation nuclei (CCN) and ice nuclei (IN), altering the cloud's formation and radiative properties and, therefore, the cloud radiative effect, which is subject to large uncertainty due to the heterogeneous variations of dust particle size and mineral compositions (Tsarpalis et al., 2020; Huang et al., 2019; Ou et al., 2009; Demott et al., 2003). Furthermore, the fertilization of oceanic and terrestrial ecosystems by dust-carried micro- and macro-nutrients is another key function of long-range transport dust exerted on the Earth system (Yu et al., 2015; Remer, 2006; Westberry et al., 2023).

Recent field campaigns and observational studies have revealed a critical gap in our understanding of the presence of substantially more coarse-mode dust particles in atmospheric dust layers than can be explained by sedimentation theory alone (Ryder et al., 2019; Van Der Does et al., 2018) and, therefore, often missed in climate models (Di Biagio et al., 2020; Adebiyi et al., 2023). This finding has important implications for remote sensing, as these larger particles exhibit much more significant sensitivity in the thermal infrared (TIR) spectrum compared to the visible to near-infrared (Ryder et al., 2019; Song et al., 2022). This spectral difference presents an opportunity to retrieve dust coarse-mode particle size using TIR satellite observations, complementing traditional methods using visible to near-infrared observations.

Despite this potential, current TIR-based retrieval approaches face significant challenges. Hyperspectral atmospheric sounders, such as the Atmospheric Infrared Sounder (AIRS) and the Infrared Atmospheric Sounding Interferometer (IASI), struggle with unknown dust vertical distributions, which introduce uncertainty in outgoing radiance measurements comparable to the dust optical depth itself (Pierangelo et al., 2004). This ambiguity forces simultaneous retrievals of both aerosol optical depth (AOD) and mean layer height of dust without additional particle size constraints (Cuesta et al., 2015; Klüser et al., 2015; Clarisse et al., 2019), leaving limited information content for particle size variations (Pierangelo et al., 2005). Furthermore, validating TIR retrievals proves difficult due to the lack of ground-truth measurements in this spectral region, requiring conversion of retrieved TIR AOD to visible (VIS) wavelength for comparison with observations from ground-based sun-photometers, such as the Aerosol Robotic Network (AERONET) (Zheng et al., 2024; Capelle et al., 2018). However, this conversion also depends on assumptions of particle size distribution, refractive index, and non-spherical shapes.

Recent studies have addressed the abovementioned challenges by exploiting the sensitivity of spectral differences among TIR window channels to particle size variations with the constraints of accurate dust vertical distribution retrieved by spaceborne Lidar. Zheng et al. (2023) (referred to as Z23) combined the derived dust vertical profiles from the Cloud-Aerosol Lidar with Orthogonal Polarization (CALIOP) with synergistic TIR observations from the Moderate Resolution Imaging Spectroradiometer (MODIS) to retrieve dust effective diameter in coarse mode, yielding a 10-year (2007–2017) climatological data record over global oceans.

However, the Z23 MODIS-CALIOP approach is subject to some limitations. Firstly, the retrieval is applied to the narrow track of the Cloud-Aerosol Lidar and Infrared Pathfinder Satellite Observation (CALIPSO), restricting spatial coverage and limiting application to regional and sub-seasonal dust activities. Additionally, the developed TIR retrieval in Z23 covers oceans only, while dust properties over land, especially within the source regions, have substantially larger variations requiring accurate quantification but face challenges from variable surface emissivity and skin temperature.

This study addresses these limitations by developing an improved retrieval method for dust optical depth in TIR and effective diameter using full-swath MODIS observations at 10-km resolution over both ocean and land. Our approach consists of two key advancements. First, we apply the retrieval algorithm beyond the CALIOP track by using dust vertical distributions from the climatological CALIOP profiles, which substantially expands the spatial coverage of the retrievals. Second, we extend the TIR retrieval to cover both ocean and land pixels by improving the retrieval algorithm that takes advantage of the collocated MODIS VIS AOD.

The paper is organized as follows. Section 2 describes the data and models used in the TIR retrieval algorithm; Section 3 presents our methodological improvements for retrievals over off-CALIOP-track pixels and land surfaces; Section 4 validates our results against AERONET and Marine Aerosol Network (MAN) measurements and in-situ measured particle size distributions; Section 5 analyzes the retrieval results through two distinguished dust events over North Atlantic and Namibia coast; and Section 6 presents the discussions and summary. Through this work, we aim to provide a more comprehensive characterization of atmospheric dust properties during the transport, enhancing our ability to quantify the dust life cycle and corresponding climate impacts.

2. Data and model

2.1. Observational data from MODIS and CALIOP

In this study, we primarily use the satellite observations from MODIS and CALIOP. The MODIS instruments onboard the Terra and Aqua satellites provide observations across 36 spectral channels from visible to thermal infrared wavelengths with nearly daily global coverage. Its spatial resolution ranges from 250 m to 1 km at nadir, depending on wavelength. The onboard calibration systems maintain thermal infrared measurement stability with calibration uncertainties within ±0.03 K (Xiong et al., 2009). The TIR retrieval utilizes calibrated upwelling radiances (converted to equivalent brightness temperatures) from three thermal infrared bands centered at 8.55, 11.02, and 12.03 μm, obtained directly from the MODIS Level-1B product. These "atmospheric window" bands minimize atmospheric gas interference while maintaining sensitivity to different aspects of dust optical properties.

CALIOP, a two-wavelength (532 and 1064 nm) polarization-sensitive lidar onboard CALIPSO, operated in the A-train constellation alongside Aqua until August 2018 separation into the C-train and ended in June 2023 (Winker et al., 2009; Vaughan et al., 2009). While CALIOP has a smaller spatial coverage with a 70-m cross-track footprint, it provides vertical resolution of 30 to 60 m and a 333-m along-track sampling, enabling detailed vertical profiling of aerosols and clouds. In this study, CALIOP serves a key role in constraining the vertical distribution of dust, with a method of deriving the fractional contribution of dust to the total backscatter coefficient profiles, which was described in Appendix B in Z23. Specifically, we used the 5-km aerosol profile product ("CAL_LID_L2_05kmAPro", details in Table S1 in the supplementary material) to derive the dust vertical distribution.

2.2. Pre-requisite data and models for the TIR retrieval

This study aims to report the improvements of the retrieval based on the existing algorithm, which is detailed in Z23. Thus, in this section, we briefly introduce the pre-requisite data and models in the retrieval. All pre-requisite data are listed in Table S1 in the supplementary material.

2.2.1. Atmospheric radiative transfer model

The retrieval relies on a robust radiative transfer model for calculating the outgoing TIR radiance, represented by brightness temperature (BT), at the three MODIS TIR channels. In this study, the radiative transfer calculations combine two models: the Community Radiative Transfer Model (CRTM) for atmospheric gas absorption and the Discrete Ordinate Radiative Transfer (DISORT) for dust scattering and absorption

(Stamnes et al., 1988; Han, 2006; Chen et al., 2012). CRTM calculates atmospheric gas absorptions using pre-assumed atmospheric profiles as input and outputs atmospheric optical depths. These optical depths, along with dust optical properties, are then used in DISORT to calculate brightness temperatures at three MODIS thermal infrared bands (8.55, 11.02, and 12.03 μm) at the top-of-atmosphere (TOA).

2.2.2. Assumptions of atmospheric states

To capture TIR radiative signatures from dust extinction, we must accurately calculate BTs at TOA in cloud-free and clean scenarios, determined by atmospheric thermodynamic states. Since MODIS lacks sufficient information content in TIR spectral bands to retrieve atmospheric and surface states (i.e., surface temperature and emissivity, air temperature, water vapor, and ozone concentrations), pre-assumptions about these states are necessary to disentangle radiative interactions between dust particles and their surrounding atmosphere.

In this study, we use atmospheric profiles and surface skin temperature from the fifth generation of the European Centre for Medium-Range Weather Forecasts (ECMWF) Reanalysis (ERA-5), providing $0.25^\circ \times 0.25^\circ$ spatial resolution, 1-h temporal resolution, and 36 pressure levels vertical resolution. For land surface emissivity, we use the monthly mean MODIS-retrieved surface emissivity at the three TIR bands from the MCD12C1 product that uses the Temperature Emissivity Separation (TES) algorithm (Hulley et al., 2012; Wan and Li, 1997).

Surface over dust source regions is not Lambertian and has strong angular dependence, especially for the 8.5 μm channel (Snyder et al., 1998; Labed and Stoll, 1991). Thus, the MODIS-retrieved surface emissivity has consistent viewing angles with MODIS-observed BTs at the three TIR channels, which reduces uncertainties due to the angular-specific emitted radiance. Although there are also MODIS-retrieved land surface temperatures using the TES algorithm, it is documented to be underestimated with dust at present in the daytime (Fan et al., 2018; Stante et al., 2023). In addition, the underestimation is proportional to the dust loading because dust can reduce the detected outgoing radiance, making it lower compared to that from surfaces at dust source regions, and thereby mislead the surface temperature retrieval closer to the dust layer temperature. However, the surface skin temperature from ERA-5 avoids this issue and, therefore, is considered the better option for the TIR retrieval in this study.

To evaluate the accuracy of the CRTM-DISORT calculation with the updated a priori atmospheric states and surface characteristics and estimate the improvement compared with that in Z23, we compare the calculated BTs at TOA with those measured by Aqua MODIS at the CALIOP-MODIS collocated cloud-free and clean (aerosol-free) pixels. Details of identifying cloud-free and clean pixels from CALIOP-MODIS collocation can be found in Z23 Appendix A. For each cloud-free and clean pixel, we collocated the $0.25^\circ \times 0.25^\circ$ hourly ERA-5 atmospheric profiles and surface temperature as the assumption of the atmospheric and surface states.

Table 1
The radiative closure of each band ($BT_{\lambda,obs} - BT_{\lambda,cal}$) and band difference (($BT_{\lambda1,obs} - BT_{\lambda2,obs} - (BT_{\lambda1,cal} - BT_{\lambda2,cal})$) at cloud-free and clean scenarios for the CALIOP-collocated MODIS pixels over ocean and land at daytime in 2010–2011. N represents the number of samples.

		$BT_{\lambda,obs} - BT_{\lambda,cal}$			$((BT_{\lambda1,obs} - BT_{\lambda2,obs} - (BT_{\lambda1,cal} - BT_{\lambda2,cal}))$		
TIR Band λ		8.5 μm	11 μm	12 μm	8.5 μm −12 μm	11 μm −12 μm	8.5 μm −11 μm
Ocean	Mean	0.0	0.0	0.0	0.0	0.0	0.0
N:	Peak	0.0	0.0	0.0	−0.05	0.0	−0.05
7088711	STD	0.62	0.68	0.69	0.25	0.12	0.21
Land	Mean	0.02	0.03	0.03	0.0	0.0	0.0
N:	Peak	−0.05	−0.25	−0.15	0.05	0.0	0.0
186576	STD	1.57	1.47	1.49	1.1	0.34	1.01

As shown in Table 1, the unbiased difference of BT (dBT) at the three TIR channels in the daytime for pixels over oceans and lands indicates that the CRTM-DISORT model is capable of replicating BTs at cloud-free and clean conditions compared with MODIS observation. The standard deviation (STD) of dBTs over oceans is reduced by 20 % compared with those using MERRA-2 in Z23 (Fig. A1 in Z23), demonstrating an improvement in using the assumptions of atmospheric states with a finer spatiotemporal resolution. Although the STD of dBTs over land at three bands are all over 1 K, the model-calculated BT spectral difference (BTD) agrees better with those from observed BTD with significantly lower STD as shown in Table 1, mainly due to the offset of the uncertainty contributed by the surface temperature and emissivity among three bands. Particularly, the dBTD of 11–12 μm has the lowest STDs mainly because of the similar surface emissivity at the two bands, leading to the maximal offsets of uncertainty.

In summary, we update atmospheric and surface state assumptions based on ERA5 and MODIS land surface emissivity, which provides a better calibration to the CRTM-DISORT model over oceans. For overland pixels, the reduction of uncertainty in BTD further allows us to implement the TIR retrieval for dust over multiple source regions.

2.2.3. A priori dust optical properties

The dust optical properties used in CRTM-DISORT include extinction efficiency, single scattering albedo, and asymmetry factor for the Henyey-Greenstein phase function (Henyey and Greenstein, 1941). These properties are calculated based on the assumed dust size distribution, complex refractive indices (CRI), and non-spherical shape.

Firstly, the retrieval algorithm assumes a monomodal lognormal volume size distribution for coarse-mode dust particles, with a fixed geometric standard deviation of 0.7, which agrees with the majority of model-fitted PSD from various in-situ measurements (Ryder et al., 2018; Di Biagio et al., 2021). Because of the limited sensitivity of dust extinction to the fine mode particle size distribution ($D < 1$ μm), and the greater particle size documented over dust source regions over land, the effective diameter (Deff) range is set between 2.0 and 15 μm with the upper limit of particle size in $D = 100$ μm, which represents dust size ranging from coarse mode to super-coarse mode (see Fig. S1 in the supplemental materials).

Same as that in Z23, dust refractive indices are assigned using the LW dust CRI retrieved by 19 soil samples from 9 source regions, which is published in Di Biagio et al. (2017). Assignment of dust CRIs follows the source region with fractional contribution of dust loading greater than 0.1 based on DustCOMM dataset (Kok et al., 2021). Details can be found in Appendix C in Z23. For particle shape, we adopt the spheroidal model with aspect ratio distributions from Dubovik et al. (2006), with optical properties calculated using the T-matrix method (Mishchenko et al., 1996).

Note that the spheroid assumption may not be as optimal as advanced databases that use more realistic dust shape assumptions for calculating backscatter coefficients (Saito and Yang, 2021). Furthermore, the LW CRI from Di Biagio et al. (2017) is retrieved based on spherical assumptions. Nonetheless, in the TIR retrieval, the critical optical properties are mainly the extinction coefficients, single scattering albedo, and asymmetry factor, which are demonstrated to be similar in calculations using spherical, spheroid, and other irregular dust shapes (Zheng et al., 2023; Saito et al., 2021). Additionally, the spheroid assumption allows us to use the volume-equivalent sphere diameter as the descriptor for non-spherical particle size, which is the most common definition for comparing dust particle size among various assumptions of dust morphology (Huang et al., 2021; Reid et al., 2003).

With the spheroid assumption, we further use the T-matrix method to calculate the abovementioned dust optical properties based on the dust size, refractive index and aspect ratio distributions of spheroidal dust.

2.3. The AOD at 550 nm for dust retrieved from VIS-NIR observation

Several studies have developed various methods to derive dust AOD from the AOD at 550 nm (AOD_{550nm}) retrieved using MODIS VIS-NIR observations (Kaufman et al., 2005; Ginoux et al., 2010; Pu and Ginoux, 2018; Yu et al., 2020; Yu et al., 2009). Specifically, in this study, we leverage the AOD_{550nm} as the initial guess in the optimization of the TIR retrieval, which is introduced in Section 3.1, to help increase the computational effectiveness and mitigate the multiple solutions errors in the retrieval.

Note that MODIS AOD_{550nm} over dark and bright surfaces is retrieved by the Dark Target (DT) and the Deep Blue (DB) algorithm, respectively (Lee et al., 2012; Zhou et al., 2020a; Zhou et al., 2020b). Therefore, we apply different methods in obtaining coarse-mode AOD_{550nm} as the proxy for dust AOD_{550nm} over land and ocean. For pixels over oceans, we inherit the improved DT algorithm that applies to physically detected dusty pixels using a non-spherical dust model in coarse mode (Zhou et al., 2020b). In this study, the dust-specific DT algorithm is applied for all valid cloud-free pixels (see Section 3.2), as the TIR retrieval has the natural advantage of identifying radiative signatures contributed by dust only. For overland pixels, we directly use the DB-retrieved AOD_{550nm} and further derive the coarse-mode AOD_{550nm} using the method developed in Pu and Ginoux (2018).

2.4. Ground-based and in situ measurements for retrieval evaluation

2.4.1. AERONET and MAN observations

To evaluate the retrieval results, we compare the retrieved AOD at 10 μm ($AOD_{10\mu m}$) with the AOD from global Aerosol Robotic Networks (AERONET) (Holben et al., 1998) and Maritime Aerosol Network (MAN) (Smirnov et al., 2009). Note that AERONET/MAN retrieves total AOD in the atmospheric column directly from the measured downwelling solar radiance and sky radiance, which does not specify the contribution of dust AOD to total AOD. Therefore, we need to select the AERONET/MAN AOD that has a contribution dominated by dust, which requires three selection processes here.

Firstly, we use the coarse-mode AOD at 500 nm (AOD_{500nm}) obtained from the Version 3 Spectral Deconvolution Algorithm (SDA) product as the proxy of dust AOD, as dust is dominated by coarse particles (O'neill et al., 2001). Specifically, we use the Level-2 product for AERONET to ensure the quality of cloud-free AOD. For MAN, since the observations are from multiple cruises, we used the Level-1.5 (same quality as Level-2 from AERONET) SDA SERIES product to ensure the AOD is unbiased for any particular cruise datasets.

Afterward, we applied the retrieved fine-mode fraction (FMF) below 0.3 and the Angstrom Exponent (AE) from 440 nm to 870 nm to be less than 0.6, in order to filter out the fine-mode dominated non-dust aerosols. Lastly, we filtered the AERONET/MAN sites with geolocations outside of the "dust concentrating area", which is defined as the area with the annual mean dust fraction >0.2 from the derived 10-year averaged CALIOP climatological dataset as mentioned in Section 3.1.1.

In this study, we follow Levy et al. (2013) to collocate AOD from the retrieval with that from AERONET/MAN. Specifically, for each AERONET/MAN datapoint, we search the MODIS pixels that pass the area of the circle with a radius of 27.5 km centered at the geolocation of the corresponding AERONET/MAN geolocation within 30 min of each measurement. Afterward, we average the matched MODIS pixels to obtain the collocated retrieved AOD from MODIS. By doing so, each of the AERONET/MAN AOD datapoints has the corresponding collocated MODIS-retrieved AOD.

We admit that the aforementioned selection criteria do not exhaustively exclude contributions from non-absorptive coarse-mode sea salts. However, because sea salt aerosols yield only limited TIR signatures at TOA observed by satellites as they are often confined within the atmospheric boundary layer with relatively low optical depth (Zheng et al., 2022), the retrieved $AOD_{10\mu m}$ is mainly contributed by airborne dust. Thus, we exclude the collocated pixels with $AOD_{10\mu m} = 0.0$ to reduce false comparisons with AERONET/MAN AOD contributed by marine aerosols.

2.4.2. Dust particle size distribution from in-situ measurement

For Deff, we evaluate our results through the comparison with the in-situ measurements of the dust particle size distribution from 24 field campaigns that occurred from 2000 to 2015, which are reported and analyzed in Formenti and Di Biagio (2024). Particularly, we used the Level-2b data that describes all the in-situ measurements in terms of the volume-equivalent sphere diameter, which is consistent with what is used in our retrieval.

Note that there are several differences between the in-situ measurement and the retrieved Deff. First, we choose the in-situ measured PSDs that have a full measurable range of particle size without cut-offs, which is to ensure the calculated Deff is representative of the PSD. Secondly, we calculate Deff from the in situ measured PSDs. To be consistent with the MODIS retrieval in this study, we exclude the dust PSD for $D < 1$ μm to ensure the Deff represents the coarse particles only.

Afterward, we compare the collocated retrieved Deff within both the time range and the 50-km radius of the geolocation of each of the in-situ measurements. Both the time range and geolocation of each in situ measurement can be found in the supplement in Formenti and Di Biagio (2024).

3. Description of the retrieval improvements

In this section, we present the improvements of the TIR retrieval of $AOD_{10\mu m}$ and the effective diameter upon the foundation on the along-CALIOP-track retrieval algorithm. The improved retrieval algorithm framework is summarized in Fig. 1.

3.1. The extension of the retrieval to off-CALIOP-track MODIS pixels over land and oceans

In this study, the first key improvement upon Z23 is extending TIR retrieval from MODIS-CALIOP collocated pixels to the off-CALIOP-track MODIS pixels over both land and oceans. The main challenge is the unknown vertical distributions of dust for the off-CALIOP-track MODIS pixels. There are multiple ways that have been developed in previous studies. One is finding a "neighbor" of the on-CALIOP-track dusty pixel that shares the same BT patterns and using dust vertical distributions as a proxy for the neighbor pixel (Barker et al., 2011; Chen et al., 2020). However, this method is applicable for pixels within a 10 km radius of the on-CALIOP-track pixel, which is still very limited. The second way is to approximate the instantaneous vertical distribution of dust by using the climatologically averaged vertical dust profiles for the off-CALIOP-track pixels, which could be applied to the full swath of MODIS granules, while it would cause uncertainties that need to be estimated.

3.1.1. Construction of the monthly climatological dust vertical distribution

In this study, we chose to use climatological CALIOP dust profiles for retrieving the off-MODIS-track pixels. Firstly, we derive the dust vertical distribution based on the CALIOP-observed total attenuated backscatter coefficients and the particulate depolarization ratio (PDR) at 532 nm (Yu et al., 2015a), with the a priori dust and non-dust PDR ranging from 0.2 to 0.3 and 0.02 to 0.07, respectively. Details of the method are described in Appendix B in Z23.

Secondly, we aggregate the orbit-based CALIOP dust profiles to monthly mean grid-level dust profiles with $2^\circ \times 2^\circ$ longitude-by-latitude resolution. Note that the grid-level CALIOP datasets often have $5^\circ \times 2^\circ$ resolution due to the limited spatial coverage of CALIOP footprints. To increase the representation of spatial coverage, we aggregate the monthly dust profiles using 11-year inputs of the orbit-based CALIOP dust profiles from 2007 to 2017. Fig. 2 shows the monthly mean optical

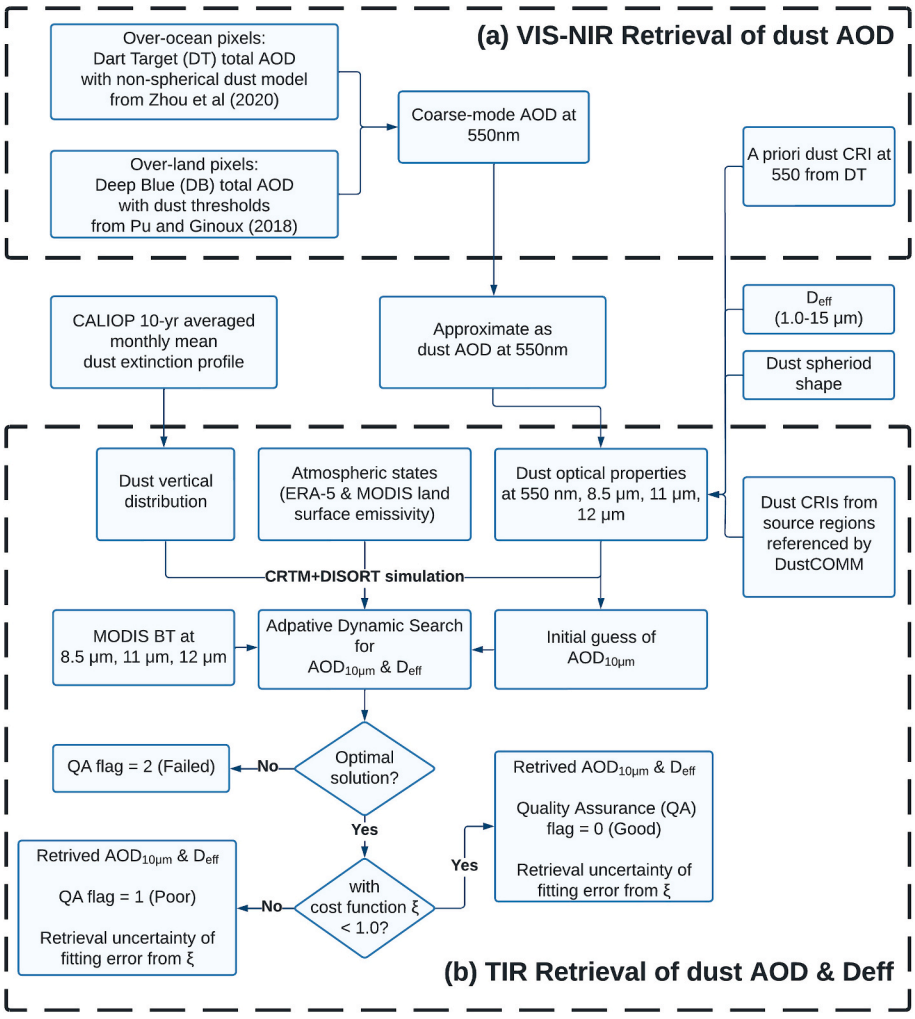

Fig. 1. The framework of the improved MODIS TIR retrieval algorithm that integrates CALIOP and MODIS visible observations.

central height, which is defined as the height above the surface topographical height with half of the optical depth below and above, from the 11-year average of CALIOP dust vertical profiles. This provides smoother spatial transitions of dust vertical profiles and, in the meantime, avoids observational gaps due to the limited coverage of CALIOP footprints.

3.1.2. *Uncertainty analysis using the monthly climatological dust profiles*

To evaluate the uncertainty due to the assumption of the climatological dust profiles, we implement the TIR retrieval following the method in Z23 for the CALIOP-collocated MODIS pixels using both the instantaneous and monthly climatological dust vertical distributions. As the retrieval in Z23 is only for observations over oceans, we first need to apply the on-CALIOP-track retrieval to overland pixels. Specifically, we inherit the retrieval method from Z23 and implement it on the overland CALIOP-MODIS collocated pixels from one-year data in 2011, with updates of atmospheric states from ERA-5 and MODIS-retrieved monthly mean surface emissivity that is described in Section 2.2. Fig. 3 shows the histogram of the retrieval difference between using the instantaneous and climatological CALIOP dust profiles of 5-km on-CALIOP-track pixel samples in June, July, and August (JJA) in 2011. We found negligible bias (Mean bias error (MBE) ~ 0.01) for both the retrieved $AOD_{10\mu m}$ and Deff from using climatological CALIOP dust vertical profiles for pixels over both land and oceans. Because of the more stable dust vertical distribution in transport regions over oceans than near source regions over land, the Root Mean Square Error (RMSE) for $AOD_{10\mu m}$ over oceans is ~50 % lower than over land. Similar results are shown in the comparison of Deff with RMSE of 0.32 for over-ocean pixels and 0.38 for overland pixels.

In addition to the pixel-by-pixel comparison, Fig. 4 shows the spatial distribution of retrieved annual mean $AOD_{10\mu m}$ and Deff in 2011 and RMSE and MBE when using the climatological CALIOP dust profiles. From Fig. 4a and b, the annual mean $AOD_{10\mu m}$ and Deff using climatological CALIOP dust profiles well capture the spatial distribution patterns compared to those of CALIOP-collocated pixels shown in Fig. 4c and d. We found that there are only limited MBE (e.g., < 0.05 in $AOD_{10\mu m}$ and < 0.5 μm in Deff) within the "dust belt" source regions, although the RMSE is noticeable (0.1–0.2 in $AOD_{10\mu m}$ and 0.5–1 μm in Deff) mainly due to the more dynamical variation of dust vertical distributions over source regions. With the promising results showing unbiased retrieval using the climatological CALIOP dust profiles, the TIR retrieval is now allowed to be implemented for off-CALIOP-track MODIS pixels.

3.2. *The pre-processing of off-CALIOP-track MODIS pixels*

For MODIS pixels in each 5-min granule, the initial step is to identify cloud-free pixels. We use the 500-m cloud mask from MYD04 aerosol product and aggregate each cloud mask into 1-km resolution with the same dimension as the MODIS L1b 1-km radiance product. The cloud fraction of 1-km pixels is defined as $f_c = \sum_4 C_{500m}/4$, where $C_{500m}$is the 500-m cloud mask. Only the 1-km pixels with $f_c = 0$ are considered

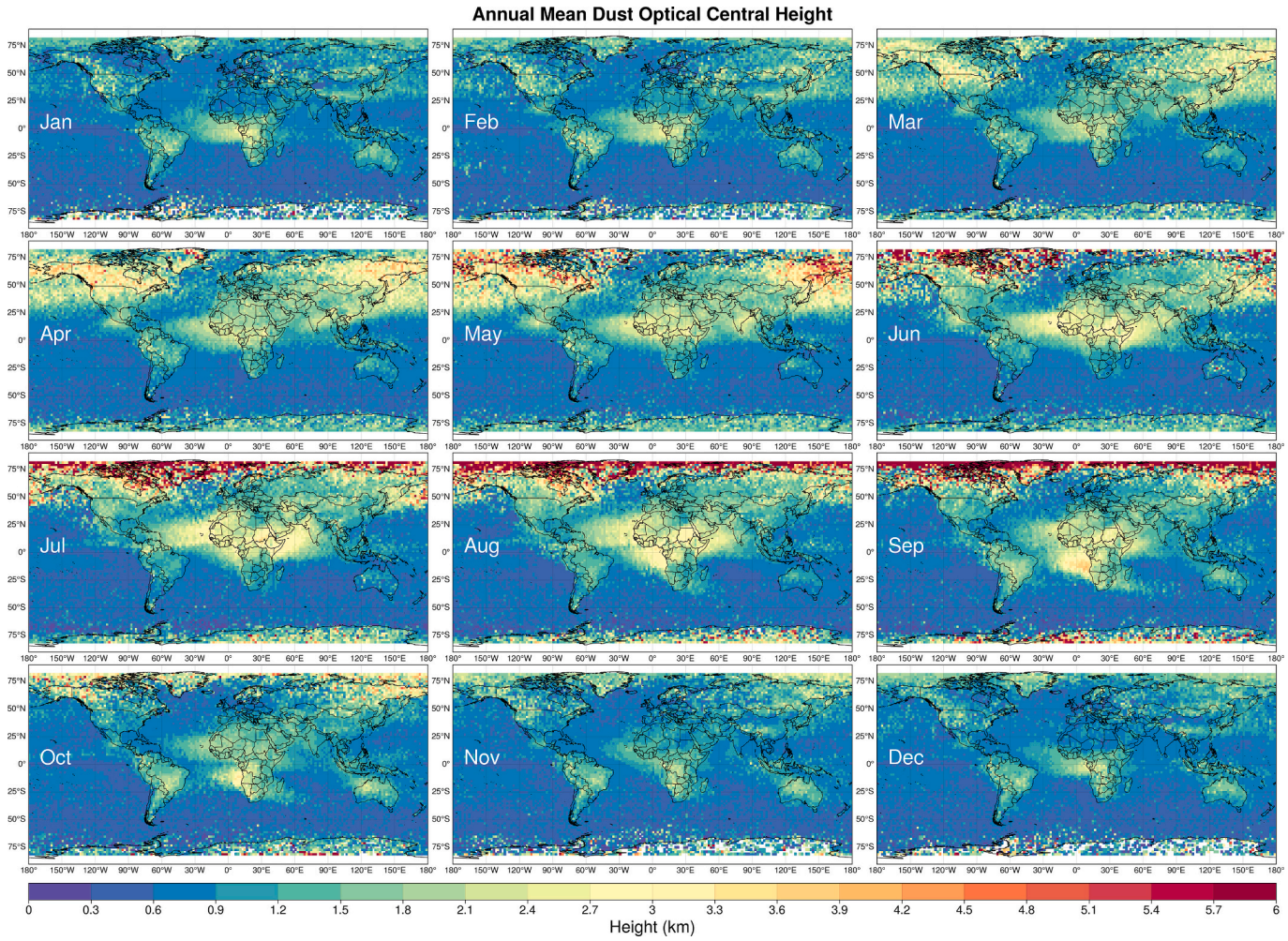

Fig. 2. The monthly mean optical central height of dust from the 10-year average of CALIOP dust vertical profiles. Optical central height is defined as the height above the surface topographical height with half of the optical depth below and above.

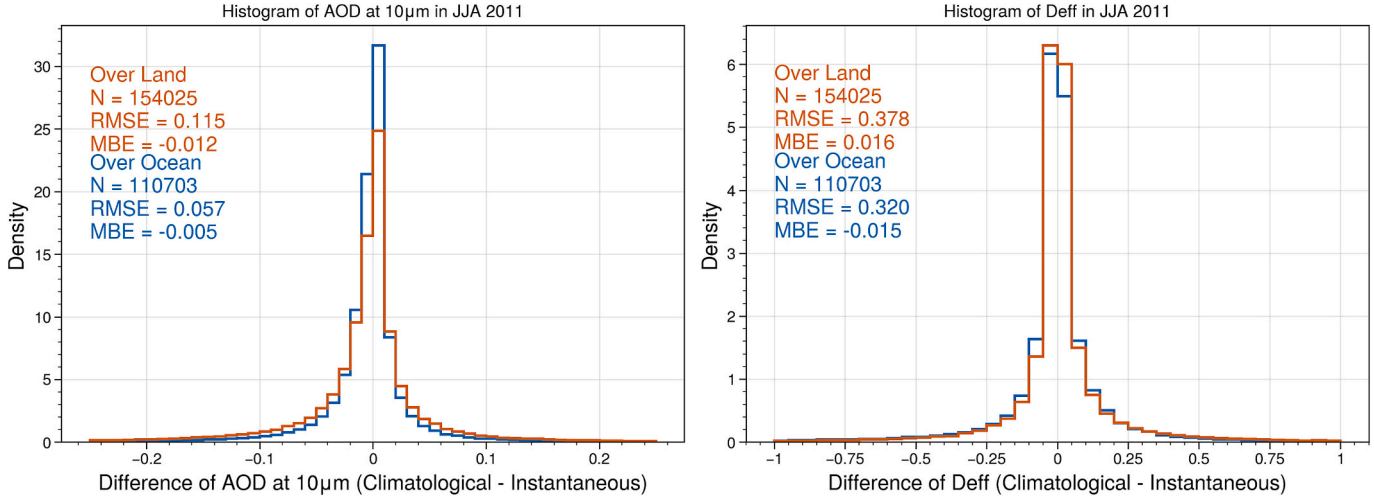

Fig. 3. The histogram of the pixel-by-pixel comparison of the AOD (left) and Deff (right) retrieval using the climatological CALIOP dust profiles with that of using the instantaneous CALIOP dust profiles from Z23 for summer (JJA) in 2011. Statistical metrics include sample size (N), root mean square error (RMSE), and mean bias error (MBE) for pixels over land (red) and oceans (blue), respectively. (For interpretation of the references to colour in this figure legend, the reader is referred to the web version of this article.)

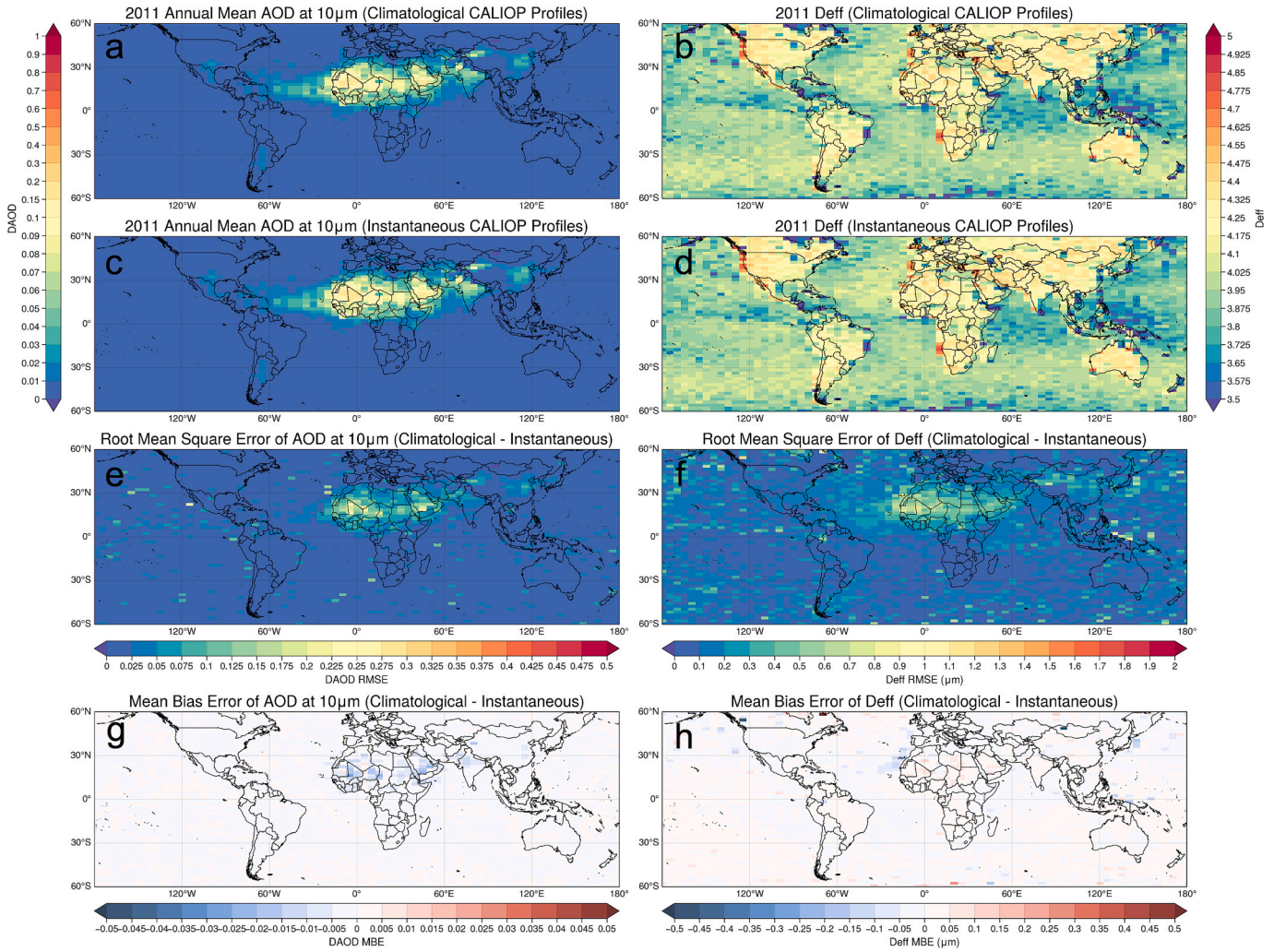

Fig. 4. The global distribution of annual mean dust AOD at 10 μm (a, c) and dust Deff (b, d) retrieved using collocated instantaneous CALIOP profiles (a, b) and 10-year averaged climatological CALIOP profiles (b, d) in 2011, along with the corresponding RMSE (e, f) and MBE (g, h) of AOD at 10 μm (e, g) and Deff (f, h) between the retrievals using instantaneous and 10-year averaged climatological CALIOP profiles as assumptions.

cloud-free pixels. Note that there still could be sub-pixel cloud contamination under the 500-m resolution, which would affect the 1-km brightness temperature (BT). Inspired by the method described in Levy et al. (2013), to reduce such effects, we exclude the 25 % highest and 25 % lowest BTs at the three TIR channels during the aggregation of 1-km pixels to 10-km pixels. The 10-km pixels also enable the synergistic use of the DT-DB aerosol products with the TIR retrieval. Lastly, we collocate the MODIS land surface emissivity, ERA-5 skin temperature and atmospheric profiles with the 10-km pixels for each 5-min MODIS granule.

Note that Z23 relies on CALIOP for detecting cloud-free dusty pixels, which is not applicable for the extended retrieval for off-CALIOP-track MODIS pixels. However, previous studies have demonstrated that dust is the only tropospheric aerosol that exerts a significant TIR radiative signature observed at TOA (Zheng et al., 2022; Zheng et al., 2023). Therefore, instead of relying on a dust detection algorithm, we implement the TIR retrieval for all available MODIS pixels that have valid retrieval from DT-DB aerosol products. The retrieved $AOD_{10\mu m}$ is the proxy of dust AOD at 10 μm, which is mainly contributed by coarse-mode dust. However, for low-AOD pixels, the information content for Deff is inadequate to obtain accurate retrieval. Thus, according to the uncertainty analysis in Z23, Deff for pixels with $AOD_{10\mu m}$ less than 0.05 is considered with low confidence in terms of quality.

3.3. The optimization method of the TIR retrieval

Due to the variation of atmospheric states and surface characteristics, the Look-Up Table (LUT) of TIR BTs will vary accordingly. Therefore, theoretically, the retrieval for each pixel requires building the LUT from scratch, which is computationally expensive, especially when applying the retrieval to off-CALIOP-track MODIS granules. Alternatively, we apply a new dynamic search approach to effectively find the optimal solution during the retrieval, which is defined as adaptive dynamic sampling.

First of all, the cost function of the optimization is defined as:

$$\xi(DAOD,Deff)=\frac{1}{N-1}\left[\frac{\left(BTD_{08-11}^{cal}-BTD_{08-11}^{obs}\right)^2}{\sigma_{08-11}^2}+\frac{\left(BTD_{11-12}^{cal}-BTD_{11-12}^{obs}\right)^2}{\sigma_{11-12}^2}+\frac{\left(BTD_{08-12}^{cal}-BTD_{08-12}^{obs}\right)^2}{\sigma_{08-12}^2}\right],$$

where.

N: the number of BTD combinations.

BTD^{cal}: The CRTM-DISORT calculated BTD combinations among BTs at 8.5, 11 and 12 μm.

BTD^{obs}: The MODIS observed BTD combinations among BT at 8.5, 11 and 12 μm.

σ: The standard deviation of the clear-sky radiative closure of the three BTDs is shown in Table 1.

We use all combinations of BTD from the three bands for the retrieval to avoid bias from any one of the bands and, in the meantime, to maximally reduce the uncertainty due to the a priori atmospheric states and surface characteristics, especially for overland pixels, as shown in Table 1. Secondly, instead of building the whole LUT with inputs of dust optical properties at the three TIR bands, we use the optimization of the Powell Conjugate Direction Method (defined as "Powell method" in the rest of the text), which is particularly useful for minimizing functions where derivatives are unavailable or expensive to compute as our retrieval does (Powell, 1964; Press, 2007). The Powell method minimizes a function by performing sequential one-dimensional minimizations along a set of directions, which allows it to periodically update the search directions to accelerate convergence.

As mentioned in Section 2.3, the LUT of TIR BTs strongly depends on the atmospheric state and surface temperatures, and emissivity. In a typical tropical atmospheric state, the contrast of BTs between the clean sky and dusty sky is easy to be captured, as shown in Z23. However, for lots of trans-Atlantic dust events, dust layers frequently transport within the Saharan Air Layer (SAL), which could have temperature inversion within the dust layers and lead to similar or even warmer dust layer temperatures than the surfaces, especially for ocean surfaces near coastal regions of North Africa (Ryder, 2021; Dunion and Velden, 2004). In these cases, dust in the warm SAL initially increases BT at TOA, but as optical depth grows, the dust obscures this warm layer, causing BT at TOA to decrease. This dual behavior creates the non-monotonic cost function and could lead to multiple solutions in the optimization.

Fig. 5a shows a synthetic example of dust within SAL in TIR retrieval. The dust layer is shown extending from near-surface to approximately 6 km altitude with concentration peaks around 1 km and 3–4 km. To perform the retrieval on this case, we set up the true value of $AOD_{10\mu m}$ = 0.25 and Deff = 5.5 μm with a given dust CRI from Mauritania in the Di Biagio Database. In this case, the temperature inversion traps the majority of the water vapor content and a portion of the dust layers within the marine boundary layer. In contrast, the drier dust layer in the free atmosphere maintains the water vapor concentration at a certain level. This unique structure diminishes the contrasts of the temperature and water vapor content between the dust layer and the surface, leading to an irregularly varied LUT and thus, an irregular cost function, as shown in Fig. 5b.

Specifically, Fig. 5b shows that there are two local minima in the cost function, one centered at $AOD_{10\mu m}$ = 0.2 and Deff from 1.5 to 2.5 μm, the other centered at around the given true value. With the traditional pre-calculated LUT method in Z23, the final solution is given by the average of all points within $\xi < 1$ weighted by ξ (see white contour line in Fig. 5b), which takes both of the local minima into account and deviates the solution from the true value. In addition, with the irregular variation of the cost function with the change of dust optical properties, calculating derivatives of BT at each TIR band is computationally expensive. Consequently, the Powell method becomes powerful for minimizing the cost function.

Note that the Powell method requires appropriate initial guesses. Therefore, we introduce the initial guess of $AOD_{10\mu m}$ constrained by AOD_{550nm} from the MODIS DT-DB retrieval. As shown in Fig. 1, AOD_{550nm} is converted to $AOD_{10\mu m}$ by $AOD_{550nm} \times Qe_{\lambda}/Qe_{550nm}$ with the given dust Deff and dust CRI. We assume Deff = 4 μm based on results in Z23. With the new initial guess, the optimization process successfully converges the iterations to the true value within the optimal solution space with the lowest cost function values (the bluish region in Fig. 5b) with only 22 iterations, as shown in the black hollow dots in Fig. 5b.

Finally, the retrieval runs for each of the assumed dust CRI in each retrieval. The final solution is the average of the best solutions with the minimum ξ from all the assumed dust CRIs. The final fitting error is the

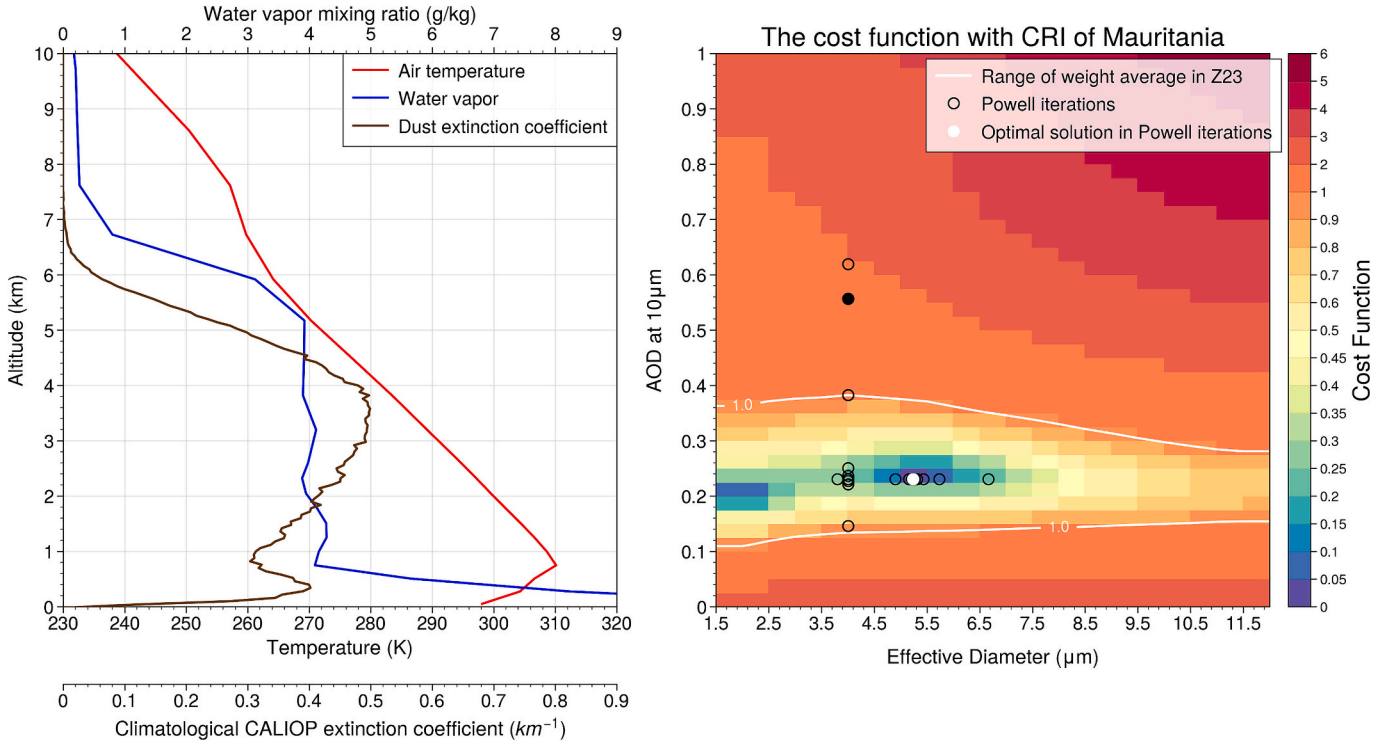

Fig. 5. (a) Vertical profiles of air temperature (blue line), water vapor mixing ratio (red line), and dust extinction coefficient (brown line) for a typical SAL structure from the ERA-5 reanalysis data. (b) The normalized cost function visualization for dust retrieval showing AOD at 10 μm versus the effective diameter (μm). The colour contours represent the cost function values. White contour lines indicate the 1.0 threshold for acceptable solutions used in Z23. Black open circles show Powell iterations of the retrieval algorithm, with the white filled circle represents the optimal solution after iterations. The black filled circle indicates the initial AOD_{550nm}-inferred guess. (For interpretation of the references to colour in this figure legend, the reader is referred to the web version of this article.)

mean of ξ. The retrieval uncertainty will be further evaluated by comparing with AERONET and in-situ measured particle size distribution in the next Section.

4. Retrieval evaluations

4.1. Evaluation of TIR AOD with AERONET/MAN observations

In this section, we evaluate the retrieved $AOD_{10\mu m}$ by comparing it with the AERONET and MAN coarse-mode AOD at 500 nm (AOD_{500nm}) over both land and oceans. Fig. 6a shows the geolocations of collocated data points from AERONET/MAN observations. First of all, we collect all available AOD_{500nm} from AERONET Level-2 product in 2010–2013 and 2019–2022 for taking into account the potential interannual variation of AOD from 2010 to 2022 (red rectangles in Fig. 6a), and MAN Level-1.5 SERIES product in 2009–2022 (blue triangles in Fig. 6a). Based on the data sampling and collocation method described in Section 2.4, we found 4703 and 1673 collocated samples from AERONET and MAN, respectively. The total numbers of collocated samples from AERONET/MAN sites are aggregated to the global 10° × 10° grid box to better present the sample distributions, as shown in Fig. 6b. We found a greater sample size over North Africa and the Middle East, which are the first two largest dust source regions, while there are ~50 % smaller sample sizes in other secondary source regions, such as East Asia, but comparable with the sample sizes in main dust transport regions, such as the North Atlantic.

In Fig. 7a and b, we found $AOD_{10\mu m}$ agrees well with coarse AOD at 500 nm over both land and ocean, with $R = 0.82$ and 0.85, respectively, despite the spectral difference of AOD in such comparison, which leads to a slope of 0.60 and 0.58, reflecting the AOD ratio between $AOD_{10\mu m}$ and AOD at 500 nm. Previous studies defined the expected error (EE) of global satellite products (e.g., MODIS, VIIRS, MISR) as an envelope that contains approximately two-thirds (or 1 standard deviation) of the collocated comparisons between the satellite retrieval and AERONET (Levy et al., 2018). In this study, we inherit this definition for estimating the retrieval uncertainty. In Fig. 7, the estimated EE is $\epsilon = 15\ \% \times$ AOD

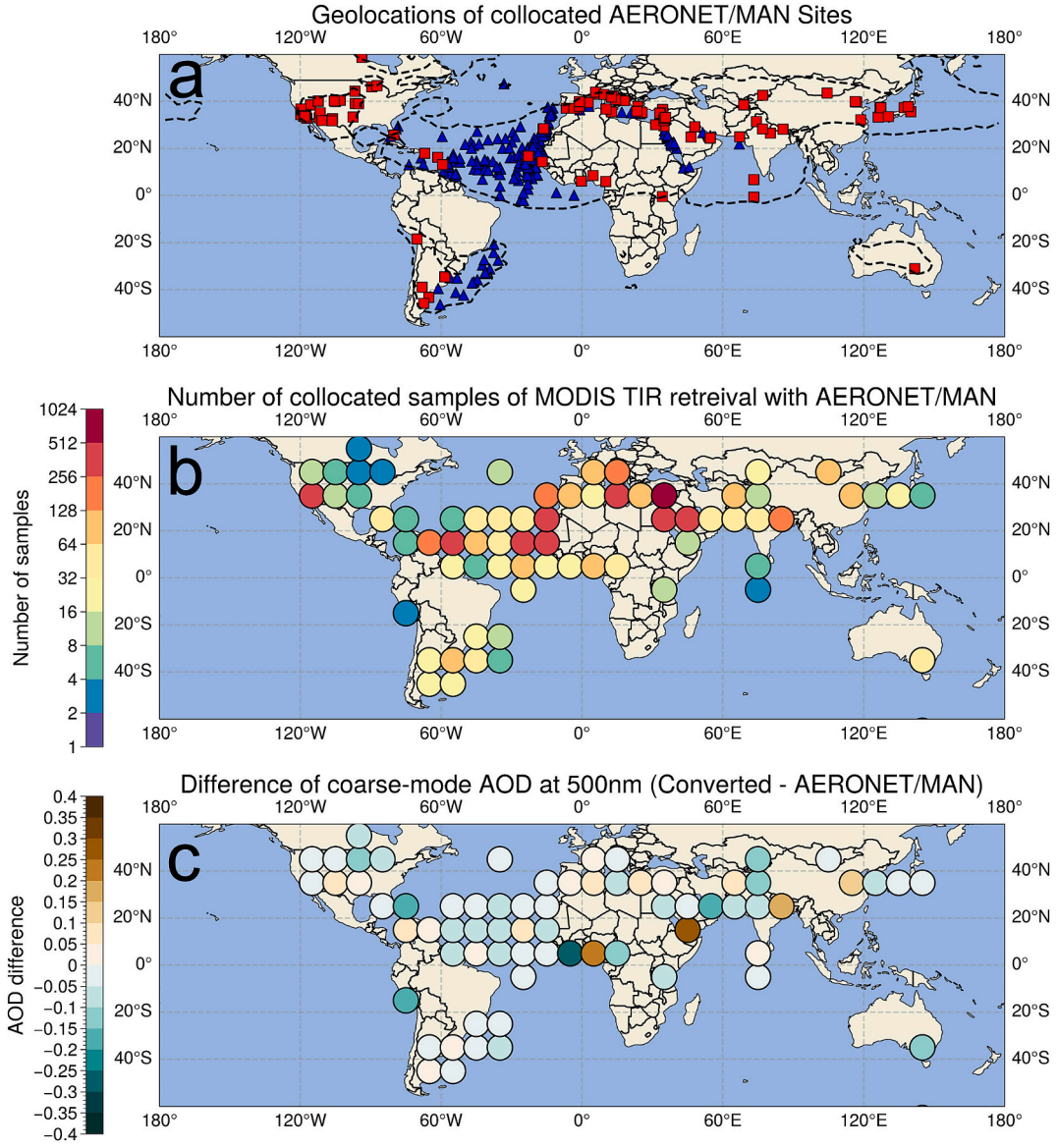

Fig. 6. (a) The geolocation of selected AERONET (2010–2013 and 2019–2022; red squares) and MAN (cruises from 2009 to 2022; blue triangles) dust-dominated sites (AE < 0.5 and FMF < 0.3) for AOD comparison. (b) The distribution of the number of collocated samples in the global 10° × 10° grid box. (c) The distribution of AOD difference between retrieval-converted AOD and AERONET AOD at 500 nm in the global 10° × 10° grid box. (For interpretation of the references to colour in this figure legend, the reader is referred to the web version of this article.)

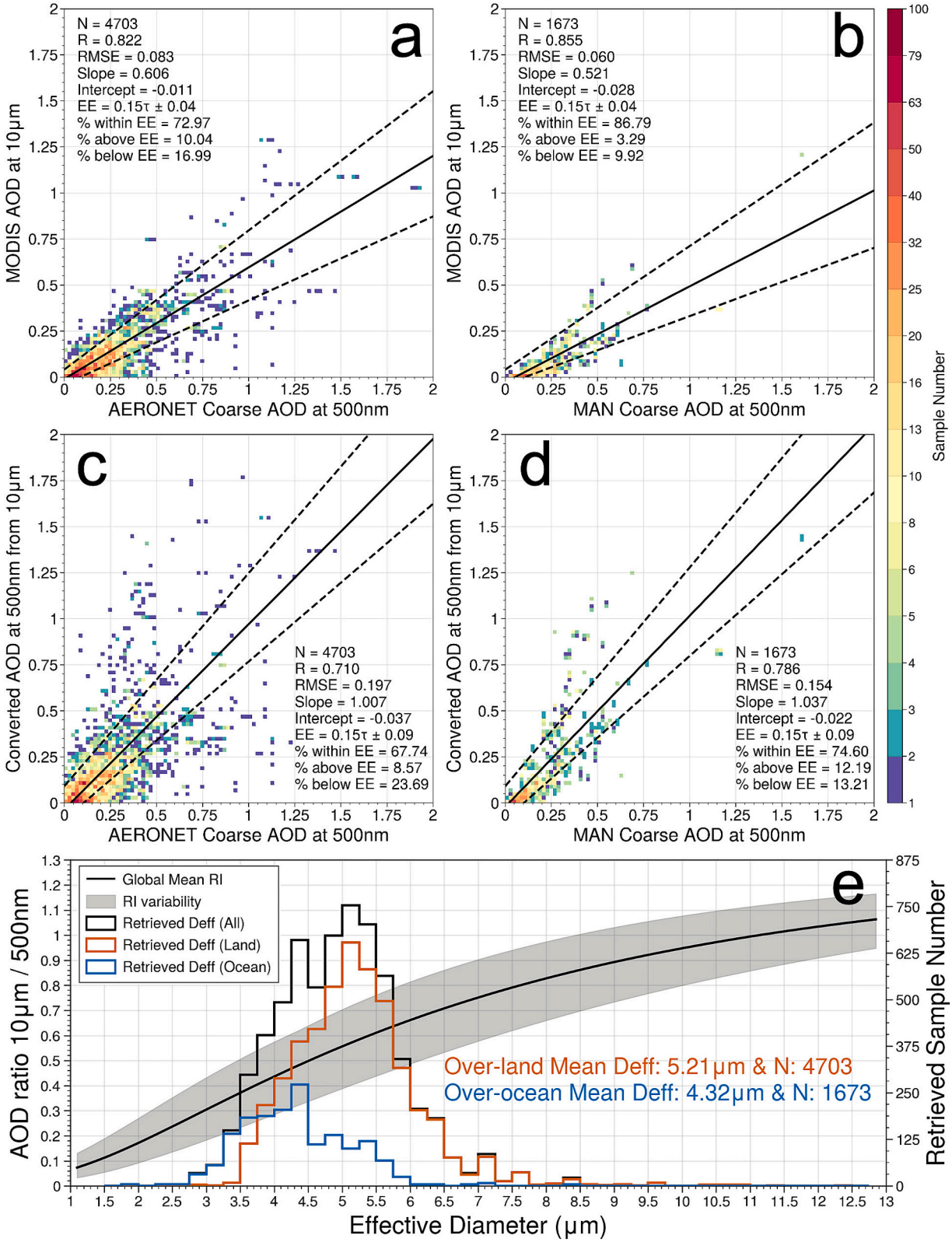

Fig. 7. The pixel-by-pixel comparison of AOD at 10 μm (a, b) and retrieval-converted AOD at 500 nm (c, d) against the collocated coarse-mode AOD at 500 nm from AERONET (a, c) and MAN (b, d). Statistical metrics include sample size (N), correlation coefficient (R), root mean square error (RMSE), slope and intercept for the linear regression (solid), and percentage of samples within, above and below the expected error (EE), respectively. (e) The AOD conversion ratio from 10 μm to 500 nm (black solid line), varied with effective diameter, calculated based on the a priori global mean dust CRI from Di Biagio et al. (2017). The grey shadow area represents the uncertainty of the AOD ratio due to the variation of dust CRI assumptions from global dust source regions. The histogram shows the retrieved Deff of the MAN/AERONET collocated samples from land (red), ocean (blue), and both (black). (For interpretation of the references to colour in this figure legend, the reader is referred to the web version of this article.)

± 0.04 (black dashed lines) with 73 % and 87 % of samples over land and oceans within the envelope. This range of uncertainty also reflects the variation of the dust AOD ratio from 10 μm to 500 nm, which is determined by dust particle size and CRI, as the two AODs are retrieved based on the spheroid assumption for dust shape. Therefore, to further evaluate the retrieval uncertainty, we calculate the 10 μm-to-500 nm AOD conversion ratio using the retrieved Deff and corresponding a priori CRIs for each of the collocated pixels as shown in Fig. 7e. The majority of Deff samples range from 3 to 6 μm, with corresponding AOD ratios from 0.2 to 0.8 with CRI uncertainty, which is consistent with the empirical range of TIR-to-VIS AOD ratios in previous studies using in-situ measurements (Highwood et al., 2003), and retrievals from AERONET (Pierangelo et al., 2004) and IASI (Peyridieu et al., 2013), ranging from 0.28 to 1.1. Note that the MAN-collocated retrieved Deff (blue histogram in Fig. 8) is systematically smaller than AERONET-collocated Deff over land, which demonstrates the decrease of dust particle size transport from source regions over land to downwind regions over oceans.

Because the Deff ranges from coarse mode ($D_{median} > 2$ μm), the converted AOD_{500nm} using the calculated AOD ratio is only contributed by coarse particles as well, which could directly compare against the AERONET/MAN coarse AOD_{500nm}. As shown in Fig. 7c and d, the converted AOD_{500nm} generally agrees with the AERONET/MAN coarse AOD_{500nm}, with $R = 0.71$ over land and 0.79 over oceans, with $\epsilon = 15\ \% \times AOD \pm 0.09$. Notably, the slope of the comparison is around 1.0, which demonstrates that the AOD ratio from the theoretical calculation based on the retrieved Deff and a priori CRI matches well with the observational AOD ratio from the retrieved $AOD_{10\mu m}$ and AERONET/MAN coarse AOD_{500nm}. In addition, we evaluate the regional variations of the mean bias of the converted AOD, which is shown in Fig. 6c. We found that the mean bias over most of dust source regions (e.g., North Africa, East Asia) and transport regions (e.g., Atlantic) is limited, while there are noticeable bias in central Africa and the foothill of Himalaya. The possible reason is that the MODIS-retrieved surface emissivity is relatively uncertain in high-cloud concentrated region in central Africa and also in regions with complicated topography such as the foothill of Himalaya. In addition, these regions also have less collocated samples (see Fig. 6b) and relatively lower coarse AOD_{500nm} than the main source regions and transport regions and, therefore, has limited impact on the overall comparison. Overall, the retrieved Deff can now constrain the AOD ratio from TIR to VIS, which is theoretically calculated or assumed in previous studies, and further lead to the constraint of the retrieved $AOD_{10\mu m}$ from the converted AOD_{500nm}.

4.2. *Evaluation of coarse-mode effective diameter with in-situ measurements*

In this section, we compare the retrieved Deff with the synthesis of in-situ measurements of dust particle size obtained from Formenti and Di Biagio (2024), with collocation and aggregation in space and time, as described in Section 2.4.2. Fig. 8b shows the geolocation of the twenty-four in situ measurements with their references denoted as numbers, which include dust measured in North Africa, North Atlantic, the Middle East, Australia and East Asia, and are categorized into three groups in terms of transport distances, near-source region (red), mid-range transport (blue), and long-range transport (green). Note that there is no valid comparison of the retrieved Deff with the in-situ PSD over source regions of East Asia (e.g., Gobi Desert) because the only available in-situ PSD in East Asia from Formenti and Di Biagio (2024) does not satisfy the comparison criteria described in Section 2.4. However, we compared the retrieved Deff with the in-situ PSD from Kobayashi et al. (2007) in Japan, which is categorized as mid-range transport dust from East Asian.

Figure 8a shows a remarkably good comparison of the retrieved Deff to the in situ Deff with $R = 0.84$, a negligible bias of MBE = 0.24 μm relative to the variation of in-situ measured Deff from 1.5 to 8 μm, and an EE of $\epsilon = 20\ \% \times$ Deff ±0.4, with about two-thirds of collocated points within the envelope. The large dynamic range of dust Deff from in-situ measurements, spanning different seasons, multiple field campaign sources, and diverse transport distances, reveals that dust particle size varies significantly with seasonal dust activities and transport distance, demonstrating the retrieval's capability in capturing the dust particle size's spatiotemporal variation in various source and

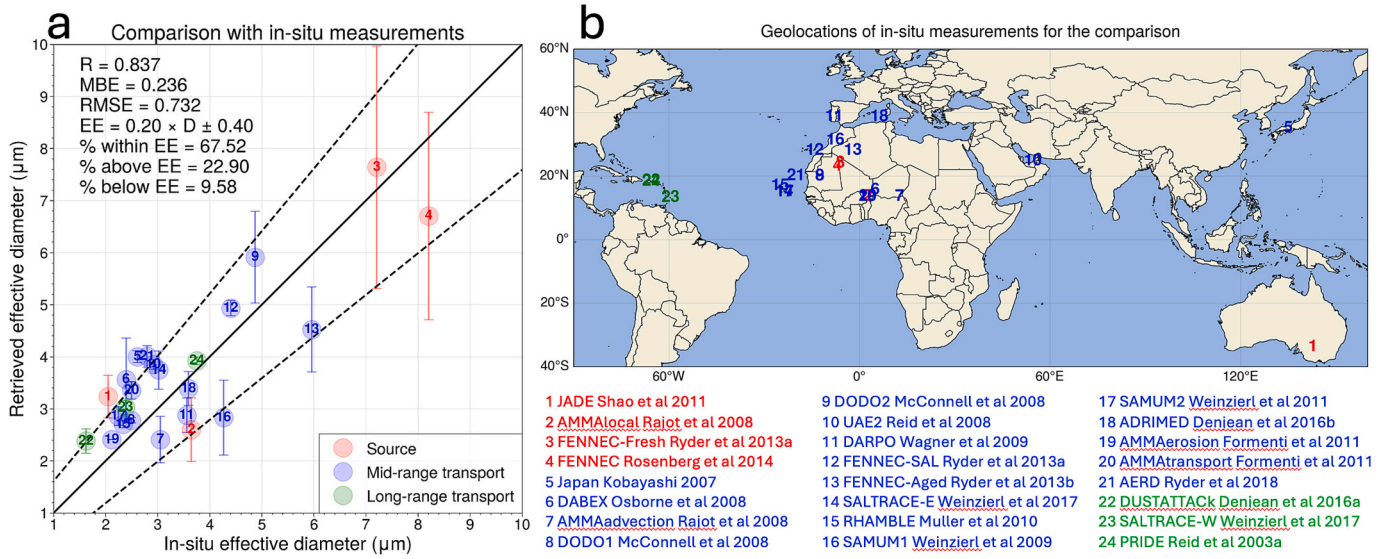

Fig. 8. The collocated comparison of retrieved Deff with multiple in-situ measurements. The in-situ effective diameter is calculated starting from D = 1 μm. (a) Scatter plot of retrieved vs. in-situ effective diameter (μm) measurements with statistical metrics and error bars representing the spatiotemporal variation of the aggregated retrieved Deff within the date range and the 50-km radius of each in-situ measurement. Data points are colour-coded by measurement source (red), mid-range transport (green), and long-range transport (blue). Statistical metrics include correlation coefficient (R), mean bias error (MBE), root mean square error (RMSE), and percentage of samples within, above, and below the expected error (EE), respectively. (b) The geographical distribution of the in-situ measurement locations used in the comparison, with numbered markers corresponding to 24 different aerosol measurement studies conducted between 2006 and 2018, as listed in the figure legend. (For interpretation of the references to colour in this figure legend, the reader is referred to the web version of this article.)

transport regions globally.

However, it is important to note that all the in-situ measurements of dust PSD are layer-specific, while the TIR-retrieved Deff represents the averaged dust size in the atmospheric column. Therefore, according to the vertical distribution of Deff from in-situ measurements in previous studies (Ryder et al., 2013; Ryder et al., 2019; Dagsson-Waldhauserova et al., 2019), there would be underestimations for comparisons with Deff that is measured in relatively low layers. Secondly, we admit that in each in-situ measurement, there are instrumental uncertainties and day-to-day variations during each field campaign. However, as mentioned in Formenti and Di Biagio (2024), it is challenging to propagate the instrumental uncertainties to the Level-2b in-situ measured dust PSD. In addition, the estimation of day-to-day variations during each field campaign highly depends on the data availability reported in the literature corresponding to the in situ measured dust PSD. Therefore, it is inapplicable for reporting uncertainties for each one-to-one comparison. Alternatively, we apply the tolerance interval of 95 % confidence level of the twenty-four comparisons, which represents the maximum uncertainty of the retrieved Deff, which is ~1.7 μm.

5. Case studies of AOD in VIS and TIR and Deff in dust events

After evaluating the retrieval of $AOD_{10\mu m}$ and Deff, we implement the retrieval for two dust events to demonstrate the ability of the retrieval in capturing the episodic variation of dust properties from source regions to transport regions.

5.1. Dust event over the Namibian coastal region

The first dust case we found is over the Namibian coastal region from July 11 to 12, 2023, which is captured by both Aqua and Terra MODIS (See True colour images in Panels a1 to a4 in Fig. 9). The dust emissions for this event originated from the Namib Desert's ephemeral river valleys and coastal sabkhas (salt flats). The distinct plume structure, as shown in Fig. 9a, demonstrates that dust was channeled offshore by the topographic configuration of the coastal mountains and valleys.

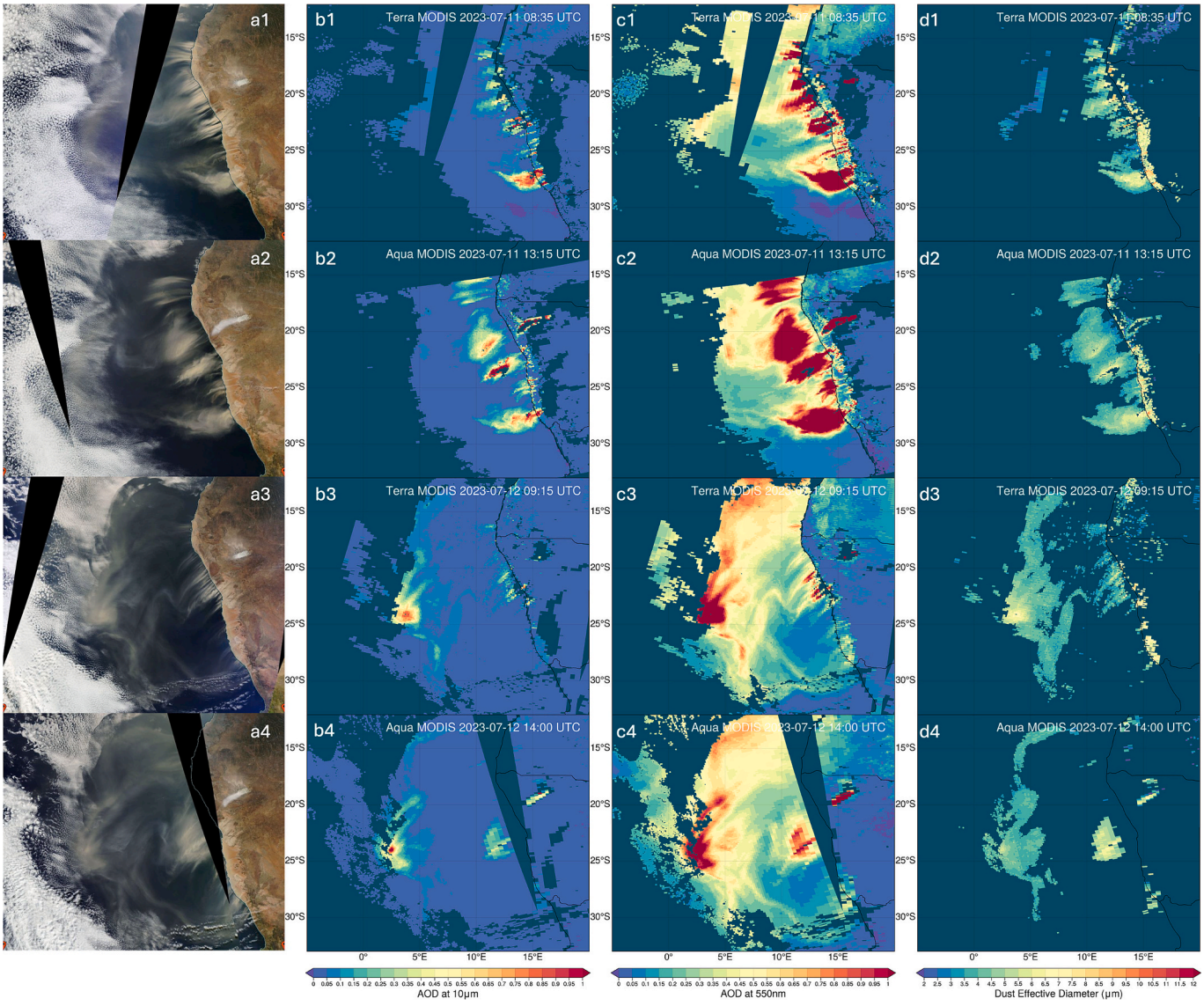

Fig. 9. Dust event over the Namibian coastal region captured by MODIS Terra and Aqua satellites from July 11–12, 2023 at four time period (rows 1–4, from top to bottom). (a) True colour MODIS images showing the visible dust plume and cloud cover. (b) Retrieved AOD at 10 μm using thermal infrared (TIR) observations, with values ranging from 0.0 to 1.0 as indicated by the colour scale. (c) MODIS Dark Target/Deep Blue (DT/dB) retrieved aerosol optical depth at 550 nm, showing the dust loading in the visible spectrum. (d) Retrieved effective diameter (Deff) for pixels with AOD at 10 μm > 0.05. The time stamps indicate the observation times in UTC for each satellite pass. (For interpretation of the references to colour in this figure legend, the reader is referred to the web version of this article.)

This event exemplifies the characteristic austral winter (June–August) dust outflows from the Namib Desert. The dust emissions for this event are primarily driven by the high-pressure system over the South Atlantic and associated strong easterly Berg winds that descend from the escarpment toward the ocean (Eckardt et al., 2013). The Namib Desert's ephemeral river valleys and dry lake beds (pans) serve as primary dust sources rather than the iconic sand dunes (Vickery and Eckardt, 2013). The dust emission patterns shown in Fig. 9a align with previously documented meteorological conditions where strong pressure gradients between the South Atlantic Anticyclone and continental low-pressure systems enhance surface winds exceeding the threshold velocity for dust mobilization (Ndarana et al., 2022; Parajuli and Zender, 2017; Maheshwarkar et al., 2024).

Fig. 9b and c show the temporal evolution of $AOD_{10\mu m}$ and AOD_{550nm}, which demonstrates how this dust event can persist while gradually dispersing over the South Atlantic. Particularly, $AOD_{10\mu m}$ shows moderate to high concentrations (0.7–1.0) near the coast, while the AOD_{550nm} reveals higher values with distinct "hot spots" of dense dust concentrations (AOD $>$ 1.0). The contrast from $AOD_{10\mu m}$ to AOD_{550nm} infers the fraction of coarse dust particles, as $AOD_{10\mu m}$ is sensitive to coarse dust only. Thus, in this event, the relatively low ratio of $AOD_{10\mu m}$ to AOD_{550nm} implies a lower burden of coarse dust. Furthermore, the effective diameter retrieval (column d) indicates moderate coarse-mode particle size (Deff from 3 to 6 μm) throughout the plume with spatial variability corresponding to that of $AOD_{10\mu m}$. Such variation suggests a differential transport mechanism, with larger particles settling closer to shore while finer dust fractions travel farther distances (Alvarez et al., 2024; Tian et al., 2020).

5.2. Trans-Atlantic dust transport of Saharan dust

In this section, we perform the retrieval for the dust event over North Africa and the North Atlantic from June 1–7, 2022, which consists of three distinct dust plumes episodically, as shown in Fig. 10.

The first plume, which is identified by the white arrows in Fig. 10, initiates from the northern Sahara/southern Atlas Mountain region on June 1–2 from 15°N to 20°N. This is the most robust and persistent plume. The $AOD_{10\mu m}$ (left column of Fig. 10) shows moderate concentrations that gradually intensify by June 3–4 as it moves westward. This plume appears to have higher Deff values (right column of Fig. 10), particularly on June 1–4, suggesting the prevalence of larger dust particles during its peak intensity. After moving from mid-Atlantic to west-Atlantic on June 5–7, $AOD_{10\mu m}$ decreases gradually from 1.2 to 0.3, while the Deff decreases from 6.8 μm to 4.4 μm on June 5 and maintains a similar value toward June 7. It shows that the dust loading for coarse particles is reducing during transport, while the particles with larger size decrease faster, and particles with moderate size deposit at a similar rate.

The second plume, which is identified by the black arrows in Fig. 10, emerges around June 3–4 between 15 and 20°N near the western African coast. The $AOD_{10\mu m}$ (left column of Fig. 10) shows it developing with moderate values (~0.7–1.0) on June 4, intensifying as it moves westward across the Atlantic. By June 5–6, this plume shows distinct separation from the first plume with consistent $AOD_{10\mu m}$ values of 0.6–0.8. The AOD_{550nm} (middle column of Fig. 10) confirms this plume maintains moderate optical thickness throughout its transport. Its Deff values (right column of Fig. 10) show a consistent range of 4.5–5.5 μm during June 4–6, without the dramatic size reduction observed in the first plume. This suggests a more stable size distribution during transport, possibly due to different emission mechanisms or vertical placement

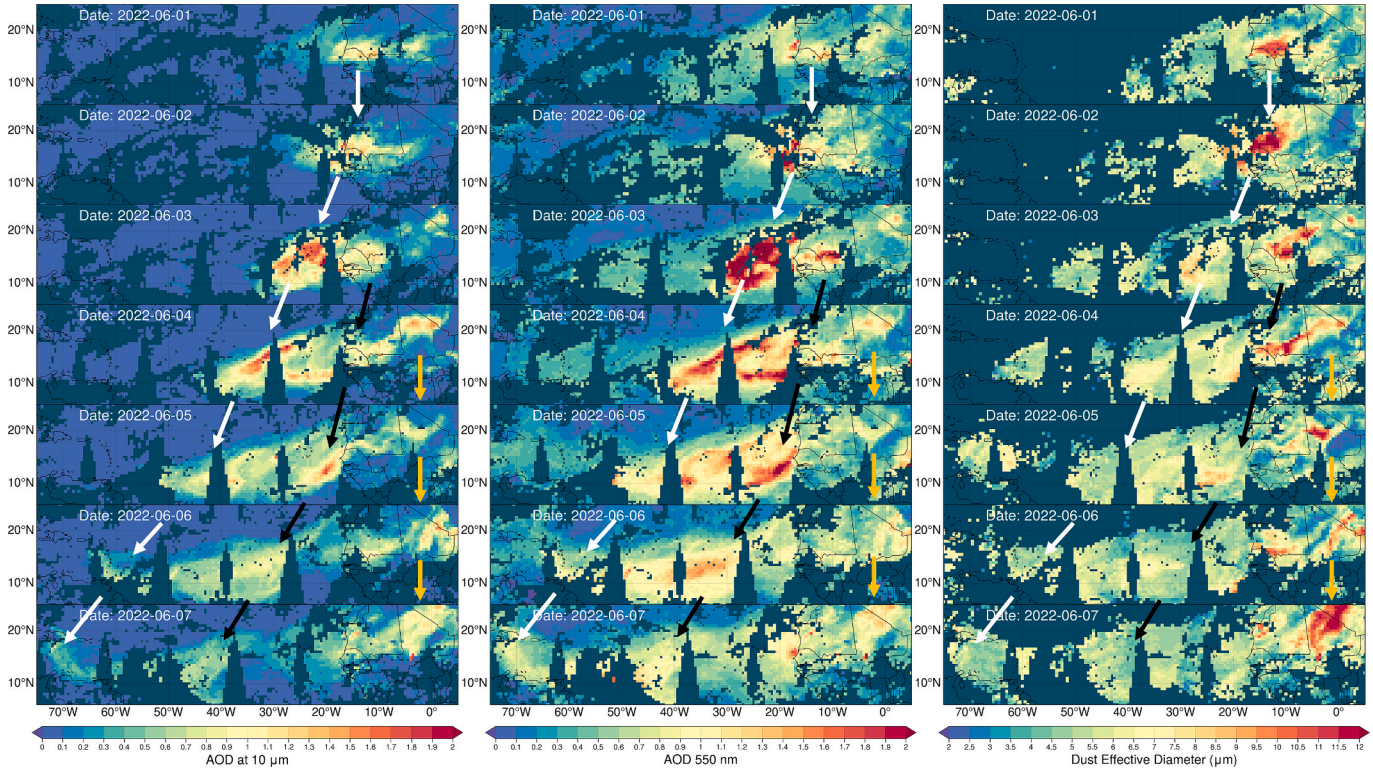

Fig. 10. The retrieval over land and ocean from MODIS Terra & Aqua for the six-day progression of African dust plumes transport across the tropical Atlantic Ocean from June 1–7, 2022. Left column: AOD at 10 μm, Middle column: AOD at 550 nm. Right column: dust effective diameter (μm) for AOD at 10 μm > 0.05. Arrows with different colors indicate the daily movement trajectory of the three dust plumes as they travel westward from the African continent. White, black, and yellow arrows for the first, second, and third plumes, respectively. (For interpretation of the references to colour in this figure legend, the reader is referred to the web version of this article.)

within the Saharan Air Layer. By June 7, this plume shows diminishing $AOD_{10\mu m}$ values (~0.4) as it continues westward beyond 50°W, while maintaining Deff around 4.0–4.5 μm, indicating the preferential deposition of larger particles has already occurred earlier in its transport cycle.

The third plume, denoted by the orange arrows in Fig. 10, appears as a distinct feature emerging from northern Mali around June 4 near 20°N. This dust plume shows relatively stable $AOD_{10\mu m}$ (~1.0–1.2) and Deff (8–10 μm) during June 4–6. It was separated into two sub-plumes, one is transported westward and the other stays within the continent. On June 7, there is a rapid increase of Deff to ~11 μm with $AOD_{10\mu m}$ at ~1.0 in Mali, implying that a new dust emission occurred from June 6 to 7, mixing with the inland dust sub-plume, and further transport eastward.

This sequence illustrates classic summer Saharan dust transport, driven by the African Easterly Jet and associated African Easterly Waves (Knippertz and Todd, 2012). The distinct plumes likely correspond to different source regions activated by local meteorological conditions, with the Bodélé Depression and western Saharan sources being particularly important contributors (Schepanski et al., 2017). The effective diameter variations across the plumes demonstrate the size-sorting that occurs during transport, with larger particles (~5–8 μm) dominating near source regions while smaller particles (~3–5 μm) persist during long-range transport (Ryder et al., 2019). With the TIR retrieval that is now capable of capturing the episodic dust events with greater spatial resolution from land to ocean, more analysis will be possible for various dust events that happen within dust source regions, which provides opportunities to further estimate dust emissions using satellite observations (Hennen et al., 2024; Todd and Cavazos-Guerra, 2016).

6. Discussion and conclusions

This study presents an improved TIR-based retrieval of $AOD_{10\mu m}$ and Deff from MODIS observations. The primary advancement is the extension from CALIOP-track-limited retrievals to full-swath MODIS coverage over both ocean and land surfaces. Firstly, it is achieved through the application of monthly climatological CALIOP dust profiles for off-CALIOP-track pixels, which is proven viable, with minimal bias introduction (MBE ~ 0.01 for $AOD_{10\mu m}$ and ~ 0.01 μm for Deff) compared to CALIOP-collocated retrievals over land and oceans. Additionally, the introduction of MODIS land surface emissivity and ERA-5 surface skin temperature enables retrievals for overland pixels. Lastly, we utilize the Powell optimization method to effectively address the challenge of non-monotonic cost functions, enabling robust and fast retrievals under challenging atmospheric conditions.

The validation against AERONET/MAN coarse-mode AOD demonstrates that the retrieved $AOD_{10\mu m}$ accurately captures the AOD variations and well-characterized uncertainties ($\varepsilon = 15\ \% \times AOD + 0.04$). The spectral conversion of AOD from 10 μm to 500 nm using the retrieved Deff and a priori dust CRI yields a slope of ~1.0 when compared against AERONET/MAN measurements, confirming that the retrieved particle size correctly constrains the spectral dependence of dust optical properties. This represents a significant improvement over previous approaches that relied on assumed size distributions for AOD spectral conversions.

The comparison with 24 in-situ measurements reveals exceptional agreement ($R = 0.84$) across a wide range of dust particle sizes (1.5–8 μm). The retrieved Deff successfully captures the documented size variations between different dust source regions and transport distances. This capability to resolve spatiotemporal variations in dust size is crucial for understanding dust life cycles and transport mechanisms (Li et al., 2022; Van Der Does et al., 2018).

The studies of the two dust cases demonstrate the retrieval's capability to monitor episodic dust events across diverse environments. The Namibian coastal event reveals the algorithm's ability to distinguish spatial variations in particle size within individual plumes. The sharp decrease of $AOD_{10\mu m}$ and Deff from the coast to open oceans implies significant deposition of dust when transported offshore and would possibly bring soluble iron, a primary nutrient for phytoplankton growth over the oceans (Desboeufs et al., 2024; Dansie et al., 2022). The trans-Atlantic case captures the progressive size-dependent deposition of dust particles. The observed decrease in both $AOD_{10\mu m}$ (from 1.2 to 0.3) and Deff (from 6.8 to 4.4 μm) during westward Atlantic transport aligns with previous in-situ observations of preferential deposition of larger particles while maintaining a longer lifetime than theoretically estimated (Ratcliffe et al., 2024; Gasteiger et al., 2017). Similar transport patterns for trans-Atlantic dust were also shown in terms of the ratio of coarse dust AOD to total AOD in VIS (Proestakis et al., 2024), as well as the dust AOD ratio from TIR to VIS (Zheng et al., 2023).

Several limitations warrant consideration for future improvements. First, the retrieval sensitivity Deff diminishes for $AOD_{10\mu m}$ below 0.05, where TIR signatures approach noise levels induced by atmospheric absorptions and surface characteristics. Second, the assumed monomodal lognormal size distribution with fixed geometric standard deviation ($\sigma = 0.7$) may not fully capture the complexity of dust populations, particularly in regions where freshly emitted and aged dust coexist. Third, while the spheroid assumption provides reasonable optical properties for TIR retrievals, more sophisticated particle morphology representations could potentially improve accuracy.

Future developments include the production of $AOD_{10\mu m}$ and Deff for the 23-year Aqua and Terra MODIS data record (2002–2024). This multi-decadal dust product would complement the VIS dust optical depth data sets developed in previous studies (e.g., Yu et al., 2019, 2020; Song et al., 2021) because VIS and TIR retrievals are sensitive to different particle sizes. The methodology developed here also provides a foundation for ongoing and future satellite missions, such as the ESA EarthCARE (Wehr et al., 2023) and the NASA AOS mission (Vane et al., 2022), demonstrating the value of TIR observations for comprehensive dust characterization.

CRediT authorship contribution statement

Jianyu Zheng: Writing – review & editing, Writing – original draft, Visualization, Validation, Software, Resources, Methodology, Investigation, Formal analysis, Data curation, Conceptualization. **Hongbin Yu:** Writing – review & editing, Visualization, Supervision, Resources, Project administration, Investigation, Funding acquisition, Conceptualization. **Yaping Zhou:** Writing – review & editing, Software, Investigation, Formal analysis, Data curation. **Yingxi Shi:** Writing – review & editing, Methodology, Investigation, Formal analysis. **Zhibo Zhang:** Writing – review & editing, Supervision, Resources, Project administration, Funding acquisition, Conceptualization. **Claudia Di Biagio:** Writing – review & editing, Validation, Resources, Investigation. **Paola Formenti:** Writing – review & editing, Validation, Resources, Investigation. **Alexander Smirnov:** Writing – review & editing, Validation, Resources.

Declaration of competing interest

The authors declare the following financial interests/personal relationships which may be considered as potential competing interests:

Co-author Zhibo Zhang. Given his role as associate editor of Remore Sensing of Environment, had no involvement in the peer review of this article and had no access to information regarding its peer review. Full responsibility for the editorial process for this article was delegated to another journal editor. If there are other authors, they declare that they have no known competing financial interests or personal relationships that could have appeared to influence the work reported in this paper.

Acknowledgements

The study was supported by NASA Earth Sciences programs, including the Making Earth System Data Records for Use in Research

Environments - MEaSUREs program managed by Dr. Lucia Tsaoussi (a project entitled “Development of a Comprehensive and Augmented Multi-Decadal Remote-Sensing Observations of Dust (CAMRO-Dust) Data Record for Earth Science Research and Applications”), the CALIPSO/CloudSat Science Team Recompete managed by Dr. David Considine, and the Cloud Credits Supplement to Enable Open Sciences for MEaSUREs and EMIT projects managed by Dr. Steven Crawford. Z.Z. acknowledge funding support from NASA (grant no. 80NSSC24K0457) and NSF (AGS-2232138). P.F. and C.D.B. received support from the DustClim project, which is part of ERA4CS, an ERA-NET project initiated by JPI Climate and funded by FORMAS (SE), DLR (DE), BMWFW (AT), IFD (DK), MINECO (ES), and ANR (FR) with co-funding from the European Union‘s Horizon program (grant no. 690462). CDB and PF also received support from the French national program LEFE/INSU (Les Enveloppes Fluides et l’Environnement/Institut National des Sciences de l’Univers) and by the OSU-EFLUVE (Observatoire des Sciences de l’Univers-Enveloppes Fluides de la Ville Ã l’Exobiologie) through dedicated research funding to the RED-DUST project, and the European Union’s Horizon 2020 research and innovation program through the EUROCHAMP-2020 Infrastructure Activity under grant agreement no. 730997. CDB was supported by the Centre National des Etudes Spatiales (CNES) and by the CNRS via the Labex L-IPSL, which is funded by the ANR (grant no. ANR-10-LABX-0018). The computations in this study were performed at the UMBC High Performance Computing Facility (HPCF). The facility is supported by the US National Science Foundation through the MRI program (grant nos. CNS-0821258 and CNS-1228778) and the SCREMS program (grant no. DMS-0821311), with substantial support from UMBC. We thank the NASA Level-1 & Atmosphere Archive and Distribution System (LAADS) Distributed Active Archive Center (DAAC), and the Langley Research Center Atmospheric Science Data Center for providing the MODIS and CALIPSO data. We also thank the AERONET/MAN projects at NASA/GSFC for providing the ground-based aerosol data.

Appendix A. Supplementary data

Supplementary data to this article can be found online at https://doi.org/10.1016/j.rse.2025.115083.

Data availability

The MODIS products are publicly accessible from the Level-1 and Atmosphere Archive & Distribution System Distributed Active Archive Center (LAADS DAAC) via https://ladsweb.modaps.eosdis.nasa.gov/archive/allData/61/. The CALIOP Level-2 5-km aerosol profile product is publicly accessible from the Atmospheric Science Data Center (ASDC) via https://asdc.larc.nasa.gov/data/CALIPSO/LID_L2_05kmAPro-Standard-V4-20/. The AERONET/MAN SDA products are publicly available at https://aeronet.gsfc.nasa.gov/new_web/index.html. The ERA5 hourly data on single levels are publicly available from https://cds.climate.copernicus.eu/datasets/reanalysis-era5-single-levels?tab=overview. The ERA5 hourly data on pressure levels are publicly available from https://cds.climate.copernicus.eu/datasets/reanalysis-era5-pressure-levels?tab=overview. The dust complex refractive index dataset provided in Di Biagio et al. (2017) is available at https://data.eurochamp.org/data-access/optical-properties/#/datasets. The database of dust size distribution provided in Formenti and Di Biagio (2024) is available in the EaSy data repository (https://www.easydata.earth/#/public/home). The MODIS-CALIOP collocated retrieval of AOD at 10 μm and effective diameter is publicly available at https://zenodo.org/records/7857132.

References

Adebiyi, A., Kok, J.F., Murray, B.J., Ryder, C.L., Stuut, J.-B.W., Kahn, R.A., Knippertz, P., Formenti, P., Mahowald, N.M., Pérez García-Pando, C., Klose, M., Ansmann, A., Samset, B.H., Ito, A., Balkanski, Y., Di Biagio, C., Romanias, M.N., Huang, Y., Meng, J., 2023. A review of coarse mineral dust in the earth system. Aeolian Res. 60, 100849. https://doi.org/10.1016/j.aeolia.2022.100849.

Alvarez, C.A., Gunn, A., Swann, C., Trimble, S.M., Ewing, R.C., Lapôtre, M.G., 2024. A.: direct measurements of dust settling velocity under low-density atmospheres using time-resolved particle image velocimetry. Geophys. Res. Lett. 51, e2024GL109958. https://doi.org/10.1029/2024GL109958.

Barker, H.W., Jerg, M.P., Wehr, T., Kato, S., Donovan, D.P., Hogan, R.J., 2011. A 3D cloud-construction algorithm for the EarthCARE satellite mission. Q. J. R. Meteorol. Soc. 137, 1042–1058. https://doi.org/10.1002/qj.824.

Capelle, V., Chédin, A., Pondrom, M., Crevoisier, C., Armante, R., Crepeau, L., Scott, N. A., 2018. Infrared dust aerosol optical depth retrieved daily from IASI and comparison with AERONET over the period 2007–2016. Remote Sens. Environ. 206, 15–32. https://doi.org/10.1016/j.rse.2017.12.008.

Chen, S., Tong, B., Dong, C., Wang, F., Chen, B., Cheng, C., Zhang, X., Liu, D., 2020. Retrievals of aerosol layer height during dust events over the taklimakan and gobi desert. J. Quant. Spectrosc. Radiat. Transf. 254, 107198. https://doi.org/10.1016/j.jqsrt.2020.107198.

Chen, Y., Han, Y., Weng, F., 2012. Comparison of two transmittance algorithms in the community radiative transfer model: application to AVHRR. J. Geophys. Res.-Atmos. 117. https://doi.org/10.1029/2011jd016656.

Choobari, O.A., Zawar-Reza, P., Sturman, A., 2014. The global distribution of mineral dust and its impacts on the climate system: a review. Atmos. Res. 138, 152–165. https://doi.org/10.1016/j.atmosres.2013.11.007.

Clarisse, L., Clerbaux, C., Franco, B., Hadji-Lazaro, J., Whitburn, S., Kopp, A.K., Hurtmans, D., Coheur, P.-F., 2019. A decadal data set of global atmospheric dust retrieved from IASI satellite measurements. J. Geophys. Res.-Atmos. 124, 1618–1647. https://doi.org/10.1029/2018JD029701.

Cuesta, J., Eremenko, M., Flamant, C., Dufour, G., Laurent, B., Bergametti, G., Höpfner, M., Orphal, J., Zhou, D., 2015. Three-dimensional distribution of a major desert dust outbreak over East Asia in march 2008 derived from IASI satellite observations. J. Geophys. Res.-Atmos. 120, 7099–7127. https://doi.org/10.1002/2014JD022406.

Dagsson-Waldhauserova, P., Renard, J.-B., Olafsson, H., Vignelles, D., Berthet, G., Verdier, N., Duverger, V., 2019. Vertical distribution of aerosols in dust storms during the Arctic winter. Sci. Rep. 9, 16122. https://doi.org/10.1038/s41598-019-51764-y.

Dansie, A.P., Thomas, D.S.G., Wiggs, G.F.S., Baddock, M.C., Ashpole, I., 2022. Plumes and blooms – locally-sourced Fe-rich aeolian mineral dust drives phytoplankton growth off Southwest Africa. Sci. Total Environ. 829, 154562. https://doi.org/10.1016/j.scitotenv.2022.154562.

DeMott, P.J., Sassen, K., Poellot, M.R., Baumgardner, D., Rogers, D.C., Brooks, S.D., Prenni, A.J., Kreidenweis, S.M., 2003. African dust aerosols as atmospheric ice nuclei. Geophys. Res. Lett. 30.

Desboeufs, K., Formenti, P., Torres-Sánchez, R., Schepanski, K., Chaboureau, J.P., Andersen, H., Cermak, J., Feuerstein, S., Laurent, B., Klopper, D., Namwoonde, A., Cazaunau, M., Chevaillier, S., Feron, A., Mirande-Bret, C., Triquet, S., Piketh, S.J., 2024. Fractional solubility of iron in mineral dust aerosols over coastal Namibia: a link to marine biogenic emissions? Atmos. Chem. Phys. 24, 1525–1541. https://doi.org/10.5194/acp-24-1525-2024.

Di Biagio, C., Formenti, P., Balkanski, Y., Caponi, L., Cazaunau, M., Pangui, E., Journet, E., Nowak, S., Caquineau, S., Andreae, M.O., Kandler, K., Saeed, T., Piketh, S., Seibert, D., Williams, E., Doussin, J.-F., 2017. Global scale variability of the mineral dust long-wave refractive index: a new dataset of in situ measurements for climate modeling and remote sensing. Atmos. Chem. Phys. 17, 1901–1929. https://doi.org/10.5194/acp-17-1901-2017.

Di Biagio, C., Balkanski, Y., Albani, S., Boucher, O., Formenti, P., 2020. Direct radiative effect by mineral dust aerosols constrained by new microphysical and spectral optical data. Geophys. Res. Lett. 47, e2019GL086186. https://doi.org/10.1029/2019GL086186.

Di Biagio, C., Banks, J.R., Gaetani, M., 2021. Dust atmospheric transport over long distances. In: Reference Module in Earth Systems and Environmental Sciences. Elsevier. https://doi.org/10.1016/B978-0-12-818234-5.00033-X.

van der Does, M., Knippertz, P., Zschenderlein, P., Giles Harrison, R., Stuut, J.-B.W., 2018. The mysterious long-range transport of giant mineral dust particles. Sci. Adv. 4, eaau2768. https://doi.org/10.1126/sciadv.aau2768.

Dubovik, O., Sinyuk, A., Lapyonok, T., Holben, B.N., Mishchenko, M., Yang, P., Eck, T.F., Volten, H., Munoz, O., Veihelmann, B., 2006. Application of spheroid models to account for aerosol particle nonsphericity in remote sensing of desert dust. J. Geophys. Res.-Atmos. 111.

Dunion, J.P., Velden, C.S., 2004. The impact of the Saharan air layer on Atlantic tropical cyclone activity. B Am. Meteorol. Soc. 85, 353–366. https://doi.org/10.1175/bams-85-3-353.

Eckardt, F.D., Soderberg, K., Coop, L.J., Muller, A.A., Vickery, K.J., Grandin, R.D., Jack, C., Kapalanga, T.S., Henschel, J., 2013. The nature of moisture at Gobabeb, in the central Namib Desert. J. Arid Environ. 93, 7–19. https://doi.org/10.1016/j.jaridenv.2012.01.011.

Fan, X., Nie, G., Wu, H., Tang, B.-H., 2018. Estimation of land surface temperature from three thermal infrared channels of MODIS data for dust aerosol skies. Opt. Express 26, 4148–4165. https://doi.org/10.1364/OE.26.004148.
Formenti, P., Di Biagio, C., 2024. Large synthesis of in situ field measurements of the size distribution of mineral dust aerosols across their life cycles. Earth Syst. Sci. Data 16, 4995–5007. https://doi.org/10.5194/essd-16-4995-2024.
Gasteiger, J., Groß, S., Sauer, D., Haarig, M., Ansmann, A., Weinzierl, B., 2017. Particle settling and vertical mixing in the Saharan air layer as seen from an integrated model, lidar, and in situ perspective. Atmos. Chem. Phys. 17, 297–311. https://doi.org/10.5194/acp-17-297-2017.
Ginoux, P., Garbuzov, D., Hsu, N.C., 2010. Identification of anthropogenic and natural dust sources using moderate resolution imaging Spectroradiometer (MODIS) deep blue level 2 data. J. Geophys. Res.-Atmos. 115. https://doi.org/10.1029/2009jd012398.
Han, Y., 2006. JCSDA Community Radiative Transfer Model (CRTM): Version 1.
Hansen, J., Sato, M., Ruedy, R., 1997. Radiative forcing and climate response. J. Geophys. Res.-Atmos. 102, 6831–6864.
Hennen, M., Chappell, A., Webb, N.P., Schepanski, K., Baddock, M.C., Eckardt, F.D., Kandakji, T., Lee, J.A., Nobakht, M., von Holdt, J., 2024. A new framework for evaluating dust emission model development using dichotomous satellite observations of dust emission. Sci. Total Environ. 912, 169237. https://doi.org/10.1016/j.scitotenv.2023.169237.
Henyey, L.G., Greenstein, J.L., 1941. Diffuse radiation in the galaxy. Astrophys. J. 93, 70–83. https://doi.org/10.1086/144246.
Highwood, E.J., Haywood, J.M., Silverstone, M.D., Newman, S.M., Taylor, J.P., 2003. Radiative properties and direct effect of Saharan dust measured by the C-130 aircraft during Saharan dust experiment (SHADE): 2. Terrestrial spectrum. J. Geophys. Res.-Atmos. 108.
Holben, B.N., Eck, T.F., Slutsker, I., Tanré, D., Buis, J.P., Setzer, A., Vermote, E., Reagan, J.A., Kaufman, Y.J., Nakajima, T., Lavenu, F., Jankowiak, I., Smirnov, A., 1998. AERONET—A federated instrument network and data archive for aerosol characterization. Remote Sens. Environ. 66, 1–16. https://doi.org/10.1016/S0034-4257(98)00031-5.
Huang, C.-C., Chen, S.-H., Lin, Y.-C., Earl, K., Matsui, T., Lee, H.-H., Tsai, I.-C., Chen, J.-P., Cheng, C.-T., 2019. Impacts of dust–radiation versus dust–cloud interactions on the development of a modeled mesoscale convective system over North Africa. Mon. Weather Rev. 147, 3301–3326.
Huang, J., Lin, B., Minnis, P., Wang, T., Wang, X., Hu, Y., Yi, Y., Ayers, J.K., 2006. Satellite-based assessment of possible dust aerosols semi-direct effect on cloud water path over East Asia. Geophys. Res. Lett. 33. https://doi.org/10.1029/2006GL026561.
Huang, Y., Adebiyi, A.A., Formenti, P., Kok, J.F., 2021. Linking the different diameter types of Aspherical Desert dust indicates that models underestimate coarse dust emission. Geophys. Res. Lett. 48, e2020GL092054. https://doi.org/10.1029/2020GL092054.
Hulley, G.C., Hughes, C.G., Hook, S.J., 2012. Quantifying uncertainties in land surface temperature and emissivity retrievals from ASTER and MODIS thermal infrared data. J. Geophys. Res.-Atmos. 117. https://doi.org/10.1029/2012JD018506.
Kaufman, Y.J., Koren, I., Remer, L.A., Tanre, D., Ginoux, P., Fan, S., 2005. Dust transport and deposition observed from the Terra-moderate resolution imaging Spectroradiometer (MODIS) spacecraft over the Atlantic Ocean. J. Geophys. Res.-Atmos. 110. https://doi.org/10.1029/2003jd004436.
Klüser, L., Banks, J.R., Martynenko, D., Bergemann, C., Brindley, H.E., Holzer-Popp, T., 2015. Information content of space-borne hyperspectral infrared observations with respect to mineral dust properties. Remote Sens. Environ. 156, 294–309. https://doi.org/10.1016/j.rse.2014.09.036.
Knippertz, P., Todd, M.C., 2012. Mineral dust aerosols over the Sahara: meteorological controls on emission and transport and implications for modeling. Rev. Geophys. 50. https://doi.org/10.1029/2011RG000362.
Kobayashi, H., Arao, K., Murayama, T., Iokibe, K., Koga, R., Shiobara, M., 2007. High-resolution measurement of size distributions of Asian dust using a coulter multisizer. J. Atmos. Ocean. Technol. 24, 194–205. https://doi.org/10.1175/JTECH1965.1.
Kok, J.F., Adebiyi, A.A., Albani, S., Balkanski, Y., Checa-Garcia, R., Chin, M., Colarco, P. R., Hamilton, D.S., Huang, Y., Ito, A., Klose, M., Li, L., Mahowald, N.M., Miller, R.L., Obiso, V., Pérez García-Pando, C., Rocha-Lima, A., Wan, J.S., 2021. Contribution of the world's main dust source regions to the global cycle of desert dust. Atmos. Chem. Phys. 21, 8169–8193. https://doi.org/10.5194/acp-21-8169-2021.
Kok, J.F., Storelvmo, T., Karydis, V.A., Adebiyi, A.A., Mahowald, N.M., Evan, A.T., He, C., Leung, D.M., 2023. Mineral dust aerosol impacts on global climate and climate change. Nat. Rev. Earth Environ. 4, 71–86. https://doi.org/10.1038/s43017-022-00379-5.
Labed, J., Stoll, M.P., 1991. Angular variation of land surface spectral emissivity in the thermal infrared: laboratory investigations on bare soils. Int. J. Remote Sens. 12, 2299–2310. https://doi.org/10.1080/01431169108955259.
Lee, J., Kim, J., Yang, P., Hsu, N.C., 2012. Improvement of aerosol optical depth retrieval from MODIS spectral reflectance over the global ocean using new aerosol models archived from AERONET inversion data and tri-axial ellipsoidal dust database. Atmos. Chem. Phys. 12, 7087–7102. https://doi.org/10.5194/acp-12-7087-2012.
Levy, R., Mattoo, S., Munchak, L., Remer, L., Sayer, A., Patadia, F., Hsu, N., 2013. The collection 6 MODIS aerosol products over land and ocean. Atmos. Meas. Tech. 6, 2989–3034.
Levy, R.C., Mattoo, S., Sawyer, V., Shi, Y., Colarco, P.R., Lyapustin, A.I., Wang, Y., Remer, L.A., 2018. Exploring systematic offsets between aerosol products from the two MODIS sensors. Atmos. Meas. Tech. 11, 4073–4092. https://doi.org/10.5194/amt-11-4073-2018.
Li, L., Mahowald, N.M., Miller, R.L., Pérez García-Pando, C., Klose, M., Hamilton, D.S., Gonçalves Ageitos, M., Ginoux, P., Balkanski, Y., Green, R.O., Kalashnikova, O., Kok, J.F., Obiso, V., Paynter, D., Thompson, D.R., 2021. Quantifying the range of the dust direct radiative effect due to source mineralogy uncertainty. Atmos. Chem. Phys. 21, 3973–4005. https://doi.org/10.5194/acp-21-3973-2021.
Li, L., Mahowald, N.M., Kok, J.F., Liu, X., Wu, M., Leung, D.M., Hamilton, D.S., Emmons, L.K., Huang, Y., Sexton, N., Meng, J., Wan, J., 2022. Importance of different parameterization changes for the updated dust cycle modeling in the community atmosphere model (version 6.1). Geosci. Model Dev. 15, 8181–8219. https://doi.org/10.5194/gmd-15-8181-2022.
Maheshwarkar, P., Cuesta, J., Formenti, P., Lemmouchi, F., 2024. Three-dimensional distribution of aerosols of multiple types at daily scale using TROPOMI spaceborne observations. Sci. Total Environ. 955, 177037. https://doi.org/10.1016/j.scitotenv.2024.177037.
Mahowald, N., Albani, S., Kok, J.F., Engelstaeder, S., Scanza, R., Ward, D.S., Flanner, M. G., 2014. The size distribution of desert dust aerosols and its impact on the earth system. Aeolian Res. 15, 53–71. https://doi.org/10.1016/j.aeolia.2013.09.002.
Miller, R.L., Tegen, I., 1998. Climate response to soil dust aerosols. J. Clim. 11, 3247–3267. https://doi.org/10.1175/1520-0442(1998)011<3247:Crtsda>2.0.Co;2.
Mishchenko, M.I., Travis, L.D., Mackowski, D.W., 1996. T-matrix computations of light scattering by nonspherical particles: a review. J. Quant. Spectrosc. Radiat. Transf. 55, 535–575. https://doi.org/10.1016/0022-4073(96)00002-7.
Ndarana, T., Rammopo, T.S., Reason, C.J.C., Bopape, M.-J., Engelbrecht, F., Chikoore, H., 2022. Two types of ridging South Atlantic Ocean anticyclones over South Africa and the associated dynamical processes. Atmos. Res. 265, 105897. https://doi.org/10.1016/j.atmosres.2021.105897.
Ou, S.S.-C., Liou, K.-N., Wang, X., Hansell, R., Lefevre, R., Cocks, S., 2009. Satellite remote sensing of dust aerosol indirect effects on ice cloud formation. Appl. Opt. 48, 633–642.
Parajuli, S.P., Zender, C.S., 2017. Connecting geomorphology to dust emission through high-resolution mapping of global land cover and sediment supply. Aeolian Res. 27, 47–65. https://doi.org/10.1016/j.aeolia.2017.06.002.
Peyridieu, S., Chédin, A., Capelle, V., Tsamalis, C., Pierangelo, C., Armante, R., Crevoisier, C., Crépeau, L., Siméon, M., Ducos, F., Scott, N.A., 2013. Characterisation of dust aerosols in the infrared from IASI and comparison with PARASOL, MODIS, MISR, CALIOP, and AERONET observations. Atmos. Chem. Phys. 13, 6065–6082. https://doi.org/10.5194/acp-13-6065-2013.
Pierangelo, C., Chédin, A., Heilliette, S., Jacquinet-Husson, N., Armante, R., 2004. Dust altitude and infrared optical depth from AIRS. Atmos. Chem. Phys. 4, 1813–1822. https://doi.org/10.5194/acp-4-1813-2004.
Pierangelo, C., Mishchenko, M., Balkanski, Y., Chédin, A., 2005. Retrieving the effective radius of Saharan dust coarse mode from AIRS. Geophys. Res. Lett. 32. https://doi.org/10.1029/2005gl023425.
Powell, M.J.D., 1964. An efficient method for finding the minimum of a function of several variables without calculating derivatives. Comput. J. 7, 155–162. https://doi.org/10.1093/comjnl/7.2.155.
Press, W.H., 2007. Numerical recipes 3rd edition: The art of scientific computing. Cambridge University Press.
Proestakis, E., Gkikas, A., Georgiou, T., Kampouri, A., Drakaki, E., Ryder, C.L., Marenco, F., Marinou, E., Amiridis, V., 2024. A near-global multiyear climate data record of the fine-mode and coarse-mode components of atmospheric pure dust. Atmos. Meas. Tech. 17, 3625–3667. https://doi.org/10.5194/amt-17-3625-2024.
Pu, B., Ginoux, P., 2018. How reliable are CMIP5 models in simulating dust optical depth? Atmos. Chem. Phys. 18, 12491–12510. https://doi.org/10.5194/acp-18-12491-2018.
Ratcliffe, N.G., Ryder, C.L., Bellouin, N., Woodward, S., Jones, A., Johnson, B., Wieland, L.M., Dollner, M., Gasteiger, J., Weinzierl, B., 2024. Long-range transport of coarse mineral dust: an evaluation of the met office unified model against aircraft observations. Atmos. Chem. Phys. 24, 12161–12181. https://doi.org/10.5194/acp-24-12161-2024.
Reid, J.S., Jonsson, H.H., Maring, H.B., Smirnov, A., Savoie, D.L., Cliff, S.S., Reid, E.A., Livingston, J.M., Meier, M.M., Dubovik, O., Tsay, S.-C., 2003. Comparison of size and morphological measurements of coarse mode dust particles from Africa. J. Geophys. Res.-Atmos. 108. https://doi.org/10.1029/2002JD002485.
Remer, L.A., 2006. Dust, fertilization and sources. Environ. Res. Lett. 1, 011001. https://doi.org/10.1088/1748-9326/1/1/011001.
Ryder, C.L., 2021. Radiative effects of increased water vapor in the upper Saharan air layer associated with enhanced dustiness. J. Geophys. Res.-Atmos. 126, e2021JD034696. https://doi.org/10.1029/2021JD034696.
Ryder, C.L., Highwood, E.J., Rosenberg, P.D., Trembath, J., Brooke, J.K., Bart, M., Dean, A., Crosier, J., Dorsey, J., Brindley, H., Banks, J., Marsham, J.H., McQuaid, J. B., Sodemann, H., Washington, R., 2013. Optical properties of Saharan dust aerosol and contribution from the coarse mode as measured during the fennec 2011 aircraft campaign. Atmos. Chem. Phys. 13, 303–325. https://doi.org/10.5194/acp-13-303-2013.
Ryder, C.L., Marenco, F., Brooke, J.K., Estelles, V., Cotton, R., Formenti, P., McQuaid, J. B., Price, H.C., Liu, D., Ausset, P., Rosenberg, P.D., Taylor, J.W., Choularton, T., Bower, K., Coe, H., Gallagher, M., Crosier, J., Lloyd, G., Highwood, E.J., Murray, B. J., 2018. Coarse-mode mineral dust size distributions, composition and optical properties from AER-D aircraft measurements over the tropical eastern Atlantic. Atmos. Chem. Phys. 18, 17225–17257. https://doi.org/10.5194/acp-18-17225-2018.
Ryder, C.L., Highwood, E.J., Walser, A., Seibert, P., Philipp, A., Weinzierl, B., 2019. Coarse and giant particles are ubiquitous in Saharan dust export regions and are radiatively significant over the Sahara. Atmos. Chem. Phys. 19, 15353–15376. https://doi.org/10.5194/acp-19-15353-2019.

Saito, M., Yang, P., 2021. Advanced bulk optical models linking the backscattering and microphysical properties of mineral dust aerosol. Geophys. Res. Lett. 48, e2021GL095121. https://doi.org/10.1029/2021GL095121.

Saito, M., Yang, P., Ding, J., Liu, X., 2021. A comprehensive database of the optical properties of irregular aerosol particles for radiative transfer simulations. J. Atmos. Sci. 78, 2089–2111. https://doi.org/10.1175/jas-d-20-0338.1.

Schepanski, K., Heinold, B., Tegen, I., 2017. Harmattan, Saharan heat low, and west African monsoon circulation: modulations on the Saharan dust outflow towards the North Atlantic. Atmos. Chem. Phys. 17, 10223–10243. https://doi.org/10.5194/acp-17-10223-2017.

Smirnov, A., Holben, B.N., Slutsker, I., Giles, D.M., McClain, C.R., Eck, T.F., Sakerin, S. M., Macke, A., Croot, P., Zibordi, G., Quinn, P.K., Sciare, J., Kinne, S., Harvey, M., Smyth, T.J., Piketh, S., Zielinski, T., Proshutinsky, A., Goes, J.I., Nelson, N.B., Larouche, P., Radionov, V.F., Goloub, P., Krishna Moorthy, K., Matarrese, R., Robertson, E.J., Jourdin, F., 2009. Maritime aerosol network as a component of aerosol robotic network. J. Geophys. Res.-Atmos. 114. https://doi.org/10.1029/2008JD011257.

Snyder, W.C., Z., W., Y., Z, Feng, Y.Z., 1998. Classification-based emissivity for land surface temperature measurement from space. Int. J. Remote Sens. 19, 2753–2774. https://doi.org/10.1080/014311698214497.

Song, Q., Zhang, Z., Yu, H., Ginoux, P., Shen, J., 2021. Global Dust Optical Depth Climatology Derived from CALIOP and MODIS Aerosol Retrievals on Decadal Time Scales: Regional and Interannual Variability. Atmos. Chem. Phys. Discuss. 21 (17), 1–57. https://doi.org/10.5194/acp-21-13369-2021.

Song, Q., Zhang, Z., Yu, H., Kok, J.F., Di Biagio, C., Albani, S., Zheng, J., Ding, J., 2022. Size-resolved dust direct radiative effect efficiency derived from satellite observations. Atmos. Chem. Phys. 22, 13115–13135. https://doi.org/10.5194/acp-22-13115-2022.

Stamnes, K., Tsay, S.C., Wiscombe, W., Jayaweera, K., 1988. Numerically stable algorithm for discrete-ordinate-method radiative transfer in multiple scattering and emitting layered media. Appl. Opt. 27, 2502–2509. https://doi.org/10.1364/ao.27.002502 PMID - 20531783.

Stante, F., Ermida, S.L., DaCamara, C.C., Göttsche, F.M., Trigo, I.F., 2023. Impact of high concentrations of Saharan dust aerosols on infrared-based land surface temperature products. IEEE J. Select. Topics Appl. Earth Observ. Remote Sens. 16, 4064–4079. https://doi.org/10.1109/JSTARS.2023.3263374.

Tesfaye, M., Tsidu, G.M., Botai, J., Sivakumar, V., de W. Rautenbach, C.J., 2015. Mineral dust aerosol distributions, its direct and semi-direct effects over South Africa based on regional climate model simulation. J. Arid Environ. 114, 22–40. https://doi.org/10.1016/j.jaridenv.2014.11.002.

Tian, Y., Pan, X., Wang, Z., Wang, D., Ge, B., Liu, X., Zhang, Y., Liu, H., Lei, S., Yang, T., Fu, P., Sun, Y., Wang, Z., 2020. Transport patterns, size distributions, and depolarization characteristics of dust particles in East Asia in spring 2018. J. Geophys. Res.-Atmos. 125, e2019JD031752. https://doi.org/10.1029/2019JD031752.

Todd, M.C., Cavazos-Guerra, C., 2016. Dust aerosol emission over the Sahara during summertime from cloud-aerosol Lidar with orthogonal polarization (CALIOP) observations. Atmos. Environ. 128, 147–157. https://doi.org/10.1016/j.atmosenv.2015.12.037.

Tsarpalis, K., Katsafados, P., Papadopoulos, A., Mihalopoulos, N., 2020. Assessing desert dust indirect effects on cloud microphysics through a cloud nucleation scheme: a case study over the Western Mediterranean. Remote Sens 12, 3473.

Vane, D., Moran, V., Piepmeier, J., Braun, S., Kirschbaum, D., Trepte, C., Ivanco, M., 2022. The Atmosphere Observing System (AOS): A core component of NASA's Earth System Observatory (ESO). In: 2022 IEEE Aerospace Conference (AERO), 5–12 March 2022, pp. 1–7. https://doi.org/10.1109/AERO53065.2022.9843507.

Vaughan, M.A., Powell, K.A., Winker, D.M., Hostetler, C.A., Kuehn, R.E., Hunt, W.H., Getzewich, B.J., Young, S.A., Liu, Z., McGill, M.J., 2009. Fully automated detection of cloud and aerosol layers in the CALIPSO Lidar measurements. J. Atmos. Ocean. Technol. 26, 2034–2050. https://doi.org/10.1175/2009jtecha1228.1.

Vickery, K.J., Eckardt, F.D., 2013. Dust emission controls on the lower Kuiseb River valley, Central Namib. Aeolian Res. 10, 125–133. https://doi.org/10.1016/j.aeolia.2013.02.006.

Wan, Z., Li, Z.-L., 1997. A physics-based algorithm for retrieving land-surface emissivity and temperature from EOS/MODIS data. Ieee T Geosci. Remote 35, 980–996. https://doi.org/10.1109/36.602541.

Wehr, T., Kubota, T., Tzeremes, G., Wallace, K., Nakatsuka, H., Ohno, Y., Koopman, R., Rusli, S., Kikuchi, M., Eisinger, M., 2023. The EarthCARE mission–science and system overview. Atmos. Meas. Tech. 16, 3581–3608.

Westberry, T.K., Behrenfeld, M.J., Shi, Y.R., Yu, H., Remer, L.A., Bian, H., 2023. Atmospheric nourishment of global ocean ecosystems. Science 380, 515–519. https://doi.org/10.1126/science.abq5252.

Winker, D.M., Vaughan, M.A., Omar, A., Hu, Y., Powell, K.A., Liu, Z., Hunt, W.H., Young, S.A., 2009. Overview of the CALIPSO Mission and CALIOP data processing algorithms. J. Atmos. Ocean. Technol. 26, 2310–2323. https://doi.org/10.1175/2009jtecha1281.1.

Xiong, X., Wenny, B.N., Wu, A., Barnes, W.L., Salomonson, V.V., 2009. Aqua MODIS thermal emissive band on-orbit calibration, characterization, and performance. Ieee T Geosci. Remote 47, 803–814. https://doi.org/10.1109/TGRS.2008.2005109.

Yu, H., Chin, M., Remer, L.A., Kleidman, R.G., Bellouin, N., Bian, H., Diehl, T., 2009. Variability of marine aerosol fine-mode fraction and estimates of anthropogenic aerosol component over cloud-free oceans from the moderate resolution imaging Spectroradiometer (MODIS). J. Geophys. Res.-Atmos. 114. https://doi.org/10.1029/2008JD010648.

Yu, H., Chin, M., Yuan, T., Bian, H., Remer, L.A., Prospero, J.M., Omar, A., Winker, D., Yang, Y., Zhang, Y., 2015. The fertilizing role of African dust in the Amazon rainforest: a first multiyear assessment based on data from cloud-aerosol Lidar and infrared pathfinder satellite observations. Geophys. Res. Lett. 42, 1984–1991.

Yu, H., Tan, Q., Chin, M., Remer, L.A., Kahn, R.A., Bian, H., Kim, D., Zhang, Z., Yuan, T., Omar, A.H., Winker, D.M., Levy, R.C., Kalashnikova, O., Crepeau, L., Capelle, V., Chédin, A., 2019. Estimates of African dust deposition along the trans-Atlantic transit using the Decadelong record of aerosol measurements from CALIOP, MODIS, MISR, and IASI. J. Geophys. Res.-Atmos. 124, 7975–7996. https://doi.org/10.1029/2019JD030574.

Yu, H., Yang, Y., Wang, H., Tan, Q., Chin, M., Levy, R.C., Remer, L.A., Smith, S.J., Yuan, T., Shi, Y., 2020. Interannual variability and trends of combustion aerosol and dust in major continental outflows revealed by MODIS retrievals and CAM5 simulations during 2003–2017. Atmos. Chem. Phys. 20, 139–161. https://doi.org/10.5194/acp-20-139-2020.

Zheng, J., Zhang, Z., Garnier, A., Yu, H., Song, Q., Wang, C., Dubuisson, P., Di Biagio, C., 2022. The thermal infrared optical depth of mineral dust retrieved from integrated CALIOP and IIR observations. Remote Sens. Environ. 270, 112841. https://doi.org/10.1016/j.rse.2021.112841.

Zheng, J., Zhang, Z., Yu, H., Garnier, A., Song, Q., Wang, C., Di Biagio, C., Kok, J.F., Derimian, Y., Ryder, C., 2023. Thermal infrared dust optical depth and coarse-mode effective diameter over oceans retrieved from collocated MODIS and CALIOP observations. Atmos. Chem. Phys. 23, 8271–8304. https://doi.org/10.5194/acp-23-8271-2023.

Zheng, J., Zhang, Z., DeSouza-Machado, S., Ryder, C.L., Garnier, A., Di Biagio, C., Yang, P., Welton, E.J., Yu, H., Barreto, A., Gonzalez, M., 2024. Y.: assessment of dust size retrievals based on AERONET: a case study of radiative closure from visible-near-infrared to thermal infrared. Geophys. Res. Lett. 51, e2023GL106808. https://doi.org/10.1029/2023GL106808.

Zhou, Y., Levy, R.C., Remer, L.A., Mattoo, S., Espinosa, W.R., 2020a. Dust aerosol retrieval over the oceans with the MODIS/VIIRS dark target algorithm: 2. Nonspher. Dust Model, Earth Space Sci. vol. 7, e2020EA001222. https://doi.org/10.1029/2020EA001222.

Zhou, Y., Levy, R.C., Remer, L.A., Mattoo, S., Shi, Y., Wang, C., 2020b. Dust Aerosol Retrieval Over the Oceans With the MODIS/VIIRS Dark-Target Algorithm: 1. Dust Detection, Earth Space Sci. 7, e2020EA001221. https://doi.org/10.1029/2020EA001221.